3-D Printing Quantization Predistortion Applied to Sub-THz Chained-Function Filters

LIYAN ZHU[1], ROSHAN PAYAPULLI[1], SANG-HEE SHIN[1], (Member, IEEE), MANOJ STANLEY[2], (Member, IEEE), NICK M. RIDLER[2], (Fellow, IEEE), AND STEPAN LUCYSZYN[1], (Fellow, IEEE)

[1]Department of Electrical and Electronic Engineering, Imperial College London, London SW7 2AZ, U.K.
[2]Department of Electromagnetic and Electrochemical Technologies, National Physical Laboratory, Teddington TW11 0LW, U.K.

Corresponding author: Stepan Lucyszyn (s.lucyszyn@imperial.ac.uk)

ABSTRACT This paper investigates physical dimension limits associated with the low-cost, polymer-based masked stereolithography apparatus (MSLA) 3-D printer, with 50 μm pixels defining the minimum print feature size. Based on the discretization properties of our MSLA 3-D printer, multi-step quantization predistortion is introduced to correct for registration errors between the CAD drawing and slicing software. This methodology is applied to G-band 5th order metal-pipe rectangular waveguide filters, where the pixel pitch has an equivalent electrical length of 8.5° at center frequency. When compared to the reference Chebyshev filter, our chained-function filter exhibits superior S-parameter measurements, with a low insertion loss of only 0.6 dB at its center frequency of 182 GHz, having a 0.9% frequency shift, and an acceptable worst-case passband return loss of 13 dB. Moreover, with measured dimensions after the 3-D printed parts have been commercially electroplated with a 50 μm thick layer of copper, the re-simulations are in good agreement with the S-parameter measurements. For the first time, systematic (quantization) errors associated with a pixel-based 3-D printer have been characterized and our robust predistortion methodology has been successfully demonstrated with an upper-millimeter-wave circuit. Indeed, we report the first polymer-based 3-D printed filters that operate above W-band. As pixel sizes continue to shrink, more resilient (sub-)THz filters with ever-higher frequencies of operation and more demanding specifications can be 3-D printed. Moreover, our work opens-up new opportunities for any pixel-based technology, which exhibits registration errors, with its application critically dependent on its minimum feature size.

INDEX TERMS Additive manufacturing, 3-D printing, millimeter-wave, G-band, WR-5, chained-function filter, rectangular waveguide, manufacturing sensitivity, quantization, predistortion.

I. INTRODUCTION

3-D printing represents one form of additive manufacturing. The first commercial 3-D printer, from 3D Systems (U.S.A.), was developed in the 1980s using a polymer-based technology [1]. Today, 3-D printing has proven itself to be attractive, in both academia and industry, due to its design flexibility, minimal waste, rapid prototyping and low cost. This emerging technology has already found its way into commercial products, where mass reduction is critical.

There are three main generic material categories associated with 3-D printing technology: (i) polymer-based, represented by fused deposition modeling (FDM),

polymer jetting (PolyJet) and stereolithography apparatus (SLA) [1]; (ii) pseudo-ceramic-based, represented by ceramic stereolithography apparatus (CSLA); and (iii) metal-based, which includes selective laser melting (SLM), micro laser sintering (MLS) and direct metal laser sintering (DMLS).

To date, a number of microwave (i.e., below 30 GHz) 3-D printed waveguide thru line, filter and horn antenna components have been reported in the open literature [2]–[4]. Indeed, examples of horn antennas and other quasi-optical components have been demonstrated at G-band (140 to 220 GHz) [5]; while THz metal-pipe rectangular waveguide (MPRWG) thru lines have been reported [6], [7].

Even with low-cost polymer-based desktop printers, the minimum print feature size can be considered to be within acceptable manufacturing dimensional tolerances with

all components at microwave frequencies and also with quasi-optical components up to *ca.* 220 GHz [5]. However, cavity resonators, used in impedance matching networks and filters, are highly sensitive to poor dimensional tolerances; inherently limiting the choice of manufacturing technologies for applications above microwave frequencies.

This paper investigates the manufacturability of G-band bandpass filters using low-cost polymer-based 3-D printing beyond its traditional capability. First, an exhaustive literature survey is undertaken for metal waveguide filters; subtractive manufacturing using micromachining (commercially available) above W-band (75 to 110 GHz) and additive manufacturing using 3-D printing (not commercially available) above the microwave band. Next, we introduce the little-known 'chained-function filter' concept, giving seed function combinations between traditional Butterworth and Chebyshev approximations, which provides a lower sensitivity to poor manufacturing tolerances (ideal for 3-D printing). In addition, this paper will focus on applying predistortion to mitigate against print quantization errors found with low-cost masked stereolithography apparatus (MSLA) 3-D printers. Fifth-order G-band filters are designed, manufactured and tested.

Here, we demonstrate the first polymer-based 3-D printed metal waveguide filters above W-band; these have the lowest recorded insertion loss, when compared to commercial micromachined and metal-based 3-D printed filters.

II. METAL WAVEGUIDE BANDPASS FILTER SURVEYS

In order to understand the practical difficulties associated with manufacturing metal waveguide filters, the results from two surveys are presented here, for both subtractive and additive manufacturing technologies. With the former, we undertook a comprehensive survey of commercial-off-the-shelf (COTS) bandpass filters, having a lower-passband cut-off frequency above W-band. To the best of our knowledge, Table 1 represents all the commercially-available products found online; although a number of companies can meet be-spoke specifications on request. Here, f_0, *FBW*, *IL* and *RL* are the respective quoted center frequency, fractional bandwidth, insertion loss and worst-case passband return loss.

Only 11 filter specifications were found from a worldwide search, and these are from only three companies (Eravant and Smiths Interconnect, both in the U.S.A., and Elmika in Lithuania). The lack of COTS filters is due to limited commercial applications that currently exist above W-band; this can in part be attributed to their high manufacturing costs.

As seen in Table 1, limited information is provided by the manufacturers for measured specifications. All the filters from Smiths Interconnect are Type I Chebyshev and their filter orders are given (in the range from 4th to 13th); while their materials and mass are not explicitly specified. In contrast, Eravant and Elmika provide the materials and mass, but do not explicitly state the filter type or their order. Only the G-band filter from Elmika has a quoted worst-case return loss measurement. We believe the reason for not providing return

loss measurements (normally quoted at W-band and lower frequencies) is due to their relatively poor performance – as a resulting of manufacturing dimensional tolerances becoming more significant at higher frequencies – as indirectly observed by the relatively high insertion loss measurements. It can also be seen from Table 1 that the materials used in micromachining are either lightweight aluminum or much heavier brass; while gold plating is almost always used in these COTS filters (as this inert material does not oxidize or tarnish, which would otherwise significantly increase the insertion loss of the filters).

Micromachining using high precision computer numerical control (CNC) milling, deep reactive-ion etching (DRIE) and SU-8 photoresist technologies can be used to manufacture filters above G-band. Two examples of 3rd order Chebyshev J-band (220 to 325 GHz) bandpass filters have been reported [12]. The first is CNC milled, with a measured center frequency of 286.6 GHz, insertion loss of 0.41 dB and worst-case return loss of 14 dB. The second uses SU-8 photoresist, with a measured center frequency of 298.6 GHz, insertion loss of 0.45 dB and worst-case return loss of 16 dB.

With additive manufacturing, we undertook a comprehensive survey of published research, available in the open literature, of 3-D printed metal waveguide filters operating at millimeter-wave frequencies (30 to 300 GHz). To the best of our knowledge, Table 2 represents all available references. Here, f_0 and *FBW* represent the target design parameters; *IL* and *RL* are the measured parameters, while Q_L corresponds to the measured loaded quality factor based on the 3 dB bandwidth.

Only 14 filters are reported, with six employing metal-based 3-D printing technologies (all since 2019) while the rest are polymer-based or ceramic-based (all since 2015); all demonstrate relatively low order filters (in the range from 2nd to 6th; half that for the COTS filters). In general, lower order filters are much less sensitive to poor dimensional tolerances and able to realize smaller fractional bandwidths (e.g., <4%).

In practice, poor dimensional tolerances become proportionally more significant with higher frequencies and/or smaller fractional bandwidths. As a result, at W-band and higher frequencies, 5th order filters can be difficult to 3-D print even with fractional bandwidths at 10%. At these higher frequencies, it can be seen that copper electroplating is employed to achieve an insertion loss of less than ~1 dB.

It can be seen, in Table 2, that all metal waveguide filters above W-band are realized using metal-based MLS 3-D printing technology – having a 30 μm spot size [22], and enhanced thermal and mechanical characteristics [23]. However, there are several challenges that currently limit metal-based 3-D printing: (i) poor surface roughness; (ii) poor effective bulk conductivity (when stainless steel is used [22], [23]); (iii) larger mass; and (iv) extremely high cost. For example, when comparing the 90 GHz polymer-based [20] and metal-based [21] filters, having the same target passband specification and filter order, the measured insertion losses are 0.4 dB and 1.0 dB, respectively; the greater surface roughness and

TABLE 1. COTS metal waveguide bandpass filters with lower-passband cut-off frequency above 110 GHz.

f_0 (GHz)	FBW (%)	IL (dB)	RL (dB)	Waveguide Type (Filter Order)	Machining Material	Plating Material	Mass (g)	Manufacturer	Ref.
120	0.83	~2.5	-	WR-08 (5th inferred)	Aluminum	Gold	11.34	Eravant (SAGE Millimeter)	[8]
121	6.61	~1.2	-	WR-08 (12th)	-	Gold	-	Smiths Interconnect (Millitech)	[9]
128	25.0	~1.0	-	WR-06 (13th)	-	Gold	-	Smiths Interconnect (Millitech)	[9]
131	13.7	~0.6	-	WR-08 (9th)	-	Gold	-	Smiths Interconnect (Millitech)	[9]
137.5	18.2	~4.5	-	WR-06 (-)	Brass	Gold	62.37	Eravant (SAGE Millimeter)	[10]
150	5.33	~1.7	-	WR-05 (4th)	-	Gold	-	Smiths Interconnect (Millitech)	[9]
164	9.76	~1.0	-	WR-05 (7th)	-	Gold	-	Smiths Interconnect (Millitech)	[9]
170.75	10.2	~1.4	-	WR-05 (11th)	-	Gold	-	Smiths Interconnect (Millitech)	[9]
180	22.2	≤3	≥14	WR-05 (-)	Copper/Brass	Silver or Gold	150	Elmika	[11]
210	9.52	~2	-	WR-05 (5th)	-	Gold	-	Smiths Interconnect (Millitech)	[9]
240	6.67	~3	-	WR-04 (7th)	-	Gold	-	Smiths Interconnect (Millitech)	[9]

lower effective bulk conductivity, associated with the latter, results in a significantly poorer insertion loss. For these reasons, polymer-based 3-D printing of upper-millimeter-wave (100 to 300 GHz) filters is the focus here.

III. CHAINED-FUNCTION FILTERS

In classical textbook filter theory, Butterworth and Chebyshev polynomials are standard approximations that define the target filter transfer functions. When compared to Butterworth filters, having the same order, Chebyshev filters exhibit steeper roll-off characteristics. However, Chebyshev filters are inherently more sensitive to manufacturing errors, due to the spectral distribution of return loss zeros across the passband [24]. This sensitivity increases with both an increase in filter order and reduction in fractional bandwidth. Conversely, Butterworth filters are less sensitive to manufacturing errors. However, their rejection performance is relatively poor; especially around the -3 dB cut-off frequencies. As a result, to provide the same level of rejection as its Chebyshev counterpart, the Butterworth filter's order must be increased.

Unlike the Butterworth and Chebyshev approximations, chained functions are generated by multiplying a certain number of low-order (seed) functions. The theory behind chained-function filters (CFFs) was first introduced in 1997 [25]. A rigorous theoretical investigation was undertaken in 2005 [26] and the optimal selection of seed function combinations was later developed in 2010 [27]. A number of different seed function combinations can exist, representing individual filter properties, for a given filter order. By employing Chebyshev polynomials, as the seed functions, CFFs can be regarded as a compromise between Butterworth

and Chebyshev filters [26]; effectively representing a tradeoff between the Butterworth's low sensitivity and the Chebyshev's steeper roll-off characteristics.

The family of CFFs provide individual filter properties for each seed function combination; some being more resilient than others to manufacturing errors. Therefore, this relatively new class of filters provides more design flexibility, helping to meet target specification for non-ideal manufacturing technologies.

Practical chained-function filters have previously been demonstrated in microstrip transmission line [28] and metal-pipe rectangular waveguides [13], [29]–[32]. In 2017, non-Chebyshev seed functions were introduced into CFFs; for example, with Legendre [33], Jacobi [34] and then elliptical [32] polynomials.

Most of the previous CFF papers [13], [25]–[32] focused on theoretical comparisons with the Chebyshev counterpart. However, to the best of our knowledge, no practical comparison has been investigated using the same target specifications, design implementation and manufacturing technology.

IV. FILTER DESIGN

Here, a 5th order G-band chained-function filter and its Chebyshev counterpart are designed, fabricated and tested; the initial target specifications include a center frequency of 183.3 GHz, a 25 dB worst-case passband return loss, and passband return loss fractional bandwidth of 9.3%. All filters are implemented in standard WR-5 metal-pipe rectangular waveguide, having internal cross-sectional dimensions of 1,295 μm × 647.5 μm. Given the small dimensional feature sizes needed for the inductive irises, 3-D printing (which includes post processing) and subsequent metal plating can

TABLE 2. Millimeter-wave 3-D printed metal waveguide bandpass filters.

f_0 (GHz)	FBW (%)	Filter Order	IL (dB)	RL (dB)	$Q_L = \dfrac{1}{3 \text{ dB } FBW}$	Split Block	Printer Technology	Plating Technology	Publication Year	Ref.
28	2.00	6th	5	22	49.4	No	DMLS (metal-based)	2 µm gold electroplating	2020	[13]
31	2.84	4th	1.53	14	32.5	No	SLM (metal-based)	Un-plated	2020	[14]
32	1.00	2nd	0.6	17	80.1	No	SLA	4 µm copper + 1 µm silver electroless plating	2017	[15]
32	3.13	4th	0.84	15	25.3	No	SLA	10 µm copper electroless plating	2020	[16]
32	13.6	5th	0.4	17	7.2	No	SLA	10 µm copper electroplating	2017	[17]
35	5.70	4th	2.4	12	16.5	No	SLA	5 µm copper electroless plating	2018	[18]
36	1.40	4th (cross-coupled)	0.5	21	63.7	H-plane	PolyJet	20 µm copper electroless plating	2019	[19]
90	11.1	5th	0.4	18	6.7	H-plane	SLA	10 µm copper electroplating	2016	[20]
90	11.1	5th	1	15	7.3	No	MLS (metal-based)	5 µm copper electroplating	2019	[21]
90	11.1	5th	1.94	18	7.0	No	MLS (metal-based)	Un-plated	2019	[21]
100	10.0	6th	0.95	11	15.8	E-plane	SLA	30 µm copper electroplating	2015	[4]
180	11.0	5th	2.96	18	7.1	No	MLS (metal-based)	Un-plated	2020	[22]
180	11.0	5th	2.9	18	7.2	No	MLS (metal-based)	Un-plated	2020	[22]
183	9.27	5th	0.55	13	5.8	H-plane	MSLA	50 µm copper electroplating	2022	**This work**
300	10.5	5th	4.7	10	8.0	E-plane	MLS (metal-based)	Un-plated	2021	[23]

be challenging if a high yield is required with the use of traditional diaphragms. An alternative approach is to employ a thick iris, having a wall thickness that is much greater than the minimum feature size offered by the 3-D printer. This requires additional electromagnetic (EM) simulation to be undertaken, in order to optimize physical dimensions, since theoretical design calculations are based on an infinitesimal wall thickness. However, a more unconventional approach is to realize an inductive iris with a transverse offset in the waveguide, as demonstrated with a thick-film substrate integrated waveguide 4th order Chebyshev bandpass filter at 180 GHz [35]; this avoids 3-D printing and plating of fine features (having low yields) and additional EM optimization.

Figure 1 shows the internal dimensions for a 5th order metal-pipe rectangular waveguide filter. The ith cavity is defined by its lengths $L_{i\vee}$ and $L_{i\wedge}$ ($i \in [1, 2, 3, 4, 5]$), where $L_{i\vee}$ represent inner lengths and $L_{i\wedge}$ represent outer lengths. $L_{1feed\vee}$ and $L_{1feed\wedge}$ represent the inner and outer feed lengths, respectively, at the input (Port 1). $L_{2feed\vee}$ and $L_{2feed\wedge}$ are the inner and outer feed lengths, respectively, at the output (Port 2). Note that associated inner and outer lengths have the same values with ideal manufacturing (i.e., after both 3-D printing and plating); this is not the case in practice. W_i ($i \in [1, 2, 3, 4, 5, 6]$) are the associated iris gap widths. a_i and b_i ($i \in [1, 2]$) are the internal aperture dimensions at the ith port, and a_i ($i \in [3, 4, 5, 6, 7, 8, 9]$) represent all widths within the filter structure. All simulations are undertaken with
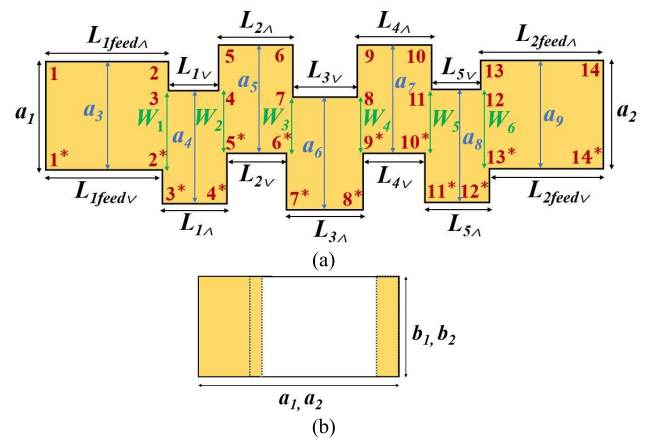
FIGURE 1. Internal dimensions for a 5th order transverse-offset inductive-iris MPRWG filter (without flanges): (a) plan view (H-plane); and (b) cross-sectional view.

commercial 3-D full-wave EM simulation software, using Ansys High-Frequency Structure Simulator (HFSS). Copper is used for the internal walls, having a conductivity of 5.8×10^7 S/m.

A. CHEBYSHEV
Following standard textbook filter synthesis [36], summarized in Appendix A, a 5th order Chebyshev bandpass filter is

TABLE 3. Polynomial coefficients of the 5th order Chebyshev filter for 25 dB worst-case passband return loss.

Polynomial Order	Polynomial Coefficients for s^i		
i	$E(s)$	$F(s)$	$P(s)$
0	1.1096	-	1.0000
1	3.2523	0.3125	-
2	4.7225	-	-
3	4.4059	1.2500	-
4	2.5124	-	-
5	1.0000	1.0000	-
Chebyshev ripple parameters: $\varepsilon_R = 1.0000$ and $\varepsilon = 0.9012$			

TABLE 4. Optimized dimensions for the 5th order Chebyshev filter (assuming ideal manufacturing).

Cavity Length, L_{i1}, L_{i2} (µm)		Iris Gap Width, W_i (µm)	
Parameter	Value	Parameter	Value
$L_{1\vee} = L_{1\wedge}$	796	W_1	832
$L_{2\vee} = L_{2\wedge}$	922	W_2	650
$L_{3\vee} = L_{3\wedge}$	942	W_3	607
$L_{4\vee} = L_{4\wedge}$	922	W_4	607
$L_{5\vee} = L_{5\wedge}$	796	W_5	650
		W_6	832

designed (the fixed polynomial function is $\psi_N(\omega) = 16\omega^5 - 20\omega^3 + 5\omega$). For a worst-case passband return loss of 25 dB, the corresponding polynomial coefficients $E(s)$, $F(s)$ and $P(s)$ are given in Table 3, where complex frequency $s = j\omega$ and ω is the angular frequency.

From the polynomials obtained using Table 3, with a filter order $N = 5$, a $(N + 2) \times (N + 2)$ prototype coupling matrix can be extracted. By applying matrix similarity transformation and annihilation [36], the final coupling matrix M_1 is given as: (1), as shown at the bottom of the next page.
Using the '*step-by-step*' design procedure [37], by adding one resonator at a time to the EM simulated model, the filter's physical dimensions are optimized (using EM simulations) and given in Table 4.

The corresponding theoretical and EM simulated responses are shown in Fig. 2, which shows excellent agreement with the characteristic five return loss zeros.
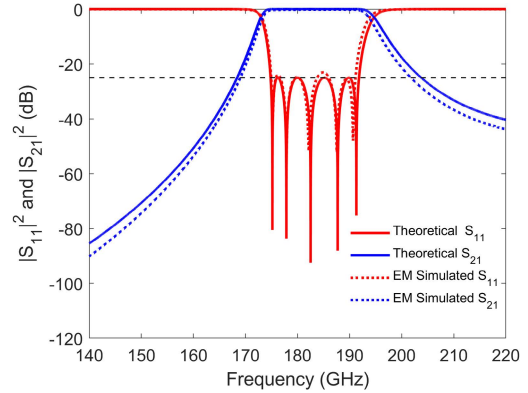
B. CHAINED FUNCTION
The chained-function polynomial $\psi_N(\omega) \equiv G_\mu(\omega)$ is formed by the combination of μ seed functions $S_{n_{s(k)}}(\omega)$ [26]:

$$G_\mu(\omega) = \prod_{k=1}^{\mu} \left(S_{n_{s(k)}}(\omega) \right)^{m_{s(k)}} \quad (2)$$

where, $n_{s(k)}$ is the order of the kth seed function, having a multiplicity of $m_{s(k)}$. The overall chained-function polynomial order N is then given as:

$$N = \sum_{k=1}^{\mu} n_{s(k)} m_{s(k)} \quad (3)$$

In this work, low-order Chebyshev polynomials are chosen as seed functions to $N = 5$, with all possible seed function combinations given in Table 5.

FIGURE 2. Theoretical and EM simulated S-parameter responses for the G-band 5th order Chebyshev filter. The black dashed lines indicate the 25 dB return loss target design bandwidth.

TABLE 5. Seed function combinations for 5th order chained-function polynomials.

No. of Seed Functions	Seed Function Combinations	Chained-Function Polynomials, $\psi_N(\omega)$	Filter Family
5	{1, 1, 1, 1, 1}	ω^5	Butterworth
4	{1, 1, 1, 2}	$2\omega^5 - \omega^3$	**This work**
3	{1, 2, 2}	$4\omega^5 - 4\omega^3 + \omega$	
3	{1, 1, 3}	$4\omega^5 - 3\omega^3$	
2	{1, 4}	$8\omega^5 - 8\omega^3 + \omega$	
2	{2, 3}	$8\omega^5 - 10\omega^3 + 3\omega$	
1	{5}	$16\omega^5 - 20\omega^3 + 5\omega$	Chebyshev

TABLE 6. Polynomial coefficients of the 5th order {1, 1, 1, 2} chained-function filter for 25 dB worst-case passband return loss.

Polynomial Order	Polynomial Coefficients for s^i		
i	$E(s)$	$F(s)$	$P(s)$
0	8.8773	-	1.0000
1	18.2678	-	-
2	18.7952	-	-
3	11.9995	0.5000	-
4	4.7957	-	-
5	1.0000	1.0000	-
CFF ripple parameters: $\varepsilon_R = 1.0000$ and $\varepsilon = 0.1126$			

As seen in Table 5, seven seed function combinations are possible, ranging from the Butterworth approximation {1, 1, 1, 1, 1} to the Chebyshev approximation {5}. The seed function combination {1, 1, 1, 2} is adopted here, having the highest number of first-order seed functions for a chained-function polynomial. It has been found, with ∼50 EM simulations, that this Butterworth-like approximation inherently makes this combination the least sensitive to manufacturing errors; theoretically, also providing steeper roll-off characteristics when compared to a Butterworth filter. With $\psi_N(\omega) = 2\omega^5 - \omega^3$, the associated polynomial coefficients $E(s)$, $F(s)$, and $P(s)$ are calculated, given in Table 6, for a worst-case passband return loss of 25 dB.

TABLE 7. Optimized dimensions for the 5th order $\{1, 1, 1, 2\}$ chained-function filter (assuming ideal manufacturing).

Cavity Length, L_{il}, L_{i2} (μm)		Iris Gap Width, W_i (μm)	
Parameter	Value	Parameter	Value
$L_{1\vee} = L_{1\wedge}$	724	W_1	928
$L_{2\vee} = L_{2\wedge}$	877	W_2	724
$L_{3\vee} = L_{3\wedge}$	912	W_3	655
$L_{4\vee} = L_{4\wedge}$	877	W_4	655
$L_{5\vee} = L_{5\wedge}$	724	W_5	724
		W_6	928

FIGURE 3. Theoretical and EM simulated S-parameter responses for the G-band 5th order $\{1, 1, 1, 2\}$ chained-function filter. The black dashed lines indicate the 25 dB return loss target design bandwidth.

After applying matrix similarity transformation and annihilation, the $(N + 2) \times (N + 2)$ prototype coupling matrix M_2 is given as: (4), as shown at the bottom of the page.
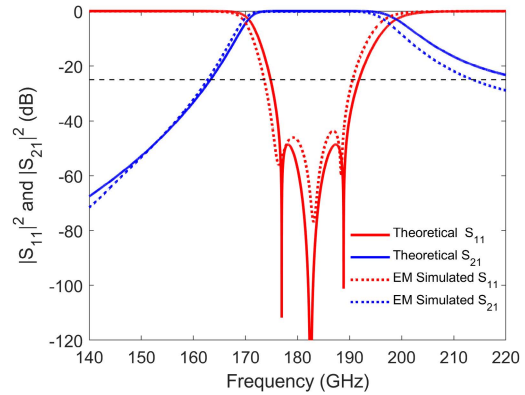
The filter's physical dimensions are optimized (using EM simulations) and given in Table 7.

The corresponding theoretical and EM simulated responses are shown in Fig. 3, which show good agreement with the three return loss zeros (the center zero corresponds to the 1st order seed functions, while the two outer zeros correspond to the 2nd order seed function). Unlike Fig. 2, which clearly exhibits the 25 dB worst-case passband return loss, the same is still true with the CFF – having peak ripples at -44 dB.

V. PIXEL-BASED 3-D PRINTING QUANTIZATION

Polymer-based 3-D printers can use a number of generic technologies for layer-by-layer printing. FDM printers are the most basic, which use a continuous thermoplastic polymer filament as the building material. Having relatively large extrusion nozzle sizes (≥ 200 μm, in most cases), FDM printers have relatively poor resolution and, therefore, are not suitable for printing G-band filters (ideally requiring sub-50 μm precision).

Material jetting printers (e.g., Stratasys' PolyJet, with a quoted *x-y* resolution of 600 dots per square inch [38]) are

very expensive and operate in a similar way to conventional 2-D inkjet printers, by spraying droplets of liquid photopolymer resin through its nozzles that is then instantly cured by an ultraviolet (UV) light source. Unlike other polymer-based 3-D printing, a wax-like material is generally deposited to support the main build structure; making it ideal for very complex geometrical features. However, since the wax-like support material requires mechanical or chemical removal, delicate structures and sharp edges are easily damaged. Moreover, residual wax-like support material cannot be electroplated; making this technology unsuitable for G-band filters.

SLA printers are expensive, because they employ scanning UV lasers (and associated precision optics) to selectively cure a layer of liquid photopolymer resin. The minimum feature size is dependent on the laser's spot size, which can be of the order of ~ 50 μm. However, sharp corners are difficult to define, mainly due to the laser's spot being circular; making this technology unsuitable for G-band filters.

$$M_1 = \begin{bmatrix} 0 & 1.1208 & 0 & 0 & 0 & 0 & 0 \\ 1.1208 & 0 & 0.9737 & 0 & 0 & 0 & 0 \\ 0 & 0.9737 & 0 & 0.6825 & 0 & 0 & 0 \\ 0 & 0 & 0.6825 & 0 & 0.6825 & 0 & 0 \\ 0 & 0 & 0 & 0.6825 & 0 & 0.9737 & 0 \\ 0 & 0 & 0 & 0 & 0.9737 & 0 & 1.1208 \\ 0 & 0 & 0 & 0 & 0 & 1.1208 & 0 \end{bmatrix} \tag{1}$$

$$M_2 = \begin{bmatrix} 0 & 1.5485 & 0 & 0 & 0 & 0 & 0 \\ 1.5485 & 0 & 1.5266 & 0 & 0 & 0 & 0 \\ 0 & 1.5266 & 0 & 0.8912 & 0 & 0 & 0 \\ 0 & 0 & 0.8912 & 0 & 0.8912 & 0 & 0 \\ 0 & 0 & 0 & 0.8912 & 0 & 1.5266 & 0 \\ 0 & 0 & 0 & 0 & 1.5266 & 0 & 1.5485 \\ 0 & 0 & 0 & 0 & 0 & 1.5485 & 0 \end{bmatrix} \tag{4}$$

With the ultra-low cost MSLA 3-D printers, an array of UV light-emitting diodes (LEDs) illuminates a programmable liquid crystal display (LCD); this acts as a shadow mask, such that UV radiation is blocked by the pixels that are turned off. The UV radiation cures the exposed liquid photopolymer resin. While there is some physical diffusion at the corners and edges of each pixel (in the *x-y* plane), clear quantization can be seen with each pixel. If this quantization can be characterized then predistortion can be introduced, to mitigate against the effects of this particular systematic manufacturing error. This section demonstrates the effects of quantization, with a specific low-cost MSLA printer, and how predistortion can be introduced in the design of G-band filters.

Autodesk Fusion 360 [39], used here, is a generic computer-aided design (CAD) drawing package and often used for designing 3-D printed parts. The output drawing file, having a standard tessellation language (STL) format, is then imported into Chitubox [40], which is a common slicing software package employed by different resin-based 3-D printers. The origin of the orthogonal coordinate axes is aligned by Chitubox to the central pixel of the LCD; the parts being printed are oriented relative to this origin (referred to here as 'registration'). With perfect registration, parts will be printed without quantization errors and so there is no need for quantization predistortion (these points will be discussed later in the next subsection). Subsequent print runs should be successful. Unfortunately, due to normal 'wear & tear' (e.g., wearing of bearings and screw threads), 3-D printers will very slowly drift and, thus, registration errors will increase with usage; until quantization errors will be evident. However, even with a brand new printer, there is no guarantee that parts will be printed without registration errors. Indeed, the chance of having negligible registration errors is very small. For this reason, our work assumes *a priori* that registration errors exist and so we have developed a design predistortion methodology to mitigate against total specification failure; instead we can now meet acceptable measured levels of performance.

A. MSLA PRINT QUANTIZATION CHARACTERIZATION

Our MSLA printer is the Elegoo Mars 2 Pro, with a quoted print volume of 80 mm × 129 mm × 160 mm [41]. This printer has a 2K monochrome LCD having a 1620 × 2560 pixel array [41]; this provides high resolution on both the *x*- and *y*-axes (giving a calculated 49.4 μm × 50.4 μm minimum feature size along the respective *x*- and *y*-axes). The vertical build *z*-axis accuracy is quoted to be 1.25 μm, for a layer thickness between 10 μm and 200 μm [41]; with our samples, the layer height is set to 20 μm. Ideally, with an MSLA printer having $\Delta = 50 \mu$m resolution in the *x-y* plane, the physical dimensions of printed pieces should be integer multiples of Δ in the *x*- and *y*-directions.

Figure 4 shows microphotographs for LCD pixels from our Elegoo Mars 2 Pro printer. It can be seen in Fig. 4(b) that each pixel can be approximated by an ellipse. The area of each pixel is calculated to be ~1,060 μm^2 and the corresponding active area is ~43%.
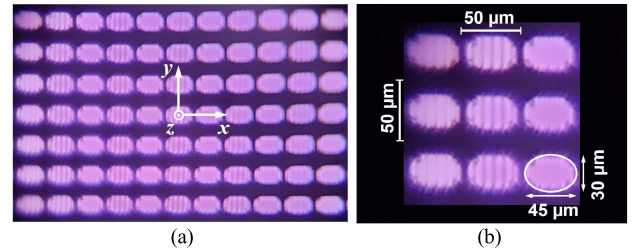
FIGURE 4. Microphotographs of LCD pixel sub-arrays with all pixels turned on (allowing UV light to pass through): (a) 11 × 7 sub-array; and (b) 3 × 3 sub-array.

A digital microscope, having a maximum magnification of ×1000, is used for visual inspection and dimension measurements. The latter is benchmarked against a reference Thorlabs calibrated standard stage micrometer; this 10 mm ruler has 50 μm divisions [42]. Note that, relatively large random errors are introduced with both the printing and measurements.

In order to characterize the quantization effects in the *x*- and *y*-directions, two different types of test prints are investigated for their physical dimensions: linear isolated small cavity arrays and single transverse offset cavities. With the former, 11 (numbered 0 to 10) equally spaced (with separation distance $\Delta l = 400 \mu$m) are distributed horizontally, as shown in Fig. 5(a).

Cavity #0 has design dimensions of 500 μm × 500 μm and acts as a reference. Cavities #1 to #5 have the same dimensions as Cavity #0, but adjacent cavities are vertically offset by 10 μm increments – this studies dimensional quantization along the vertical direction associated with its offset. Cavities #6 to #10 do not have any vertical offset from Cavity #5, but the lower boundaries of adjacent cavities are lowered by 10 μm increments (to stretch-out the cavity height) – this studies dimensional quantization along the vertical direction associated with its size.

Close-in views, representing dimensional variables, are illustrated in Fig. 5(b), where $h(i)$ represents the height of Cavity #*i*; $\Delta h_u(i)$ represents the upper boundary offset distance between Cavities #*i* and #$(i-1)$; and $\Delta h_l(i)$ represents the lower boundary offset distance between Cavities #*i* and #$(i-1)$. Table 8 gives the corresponding target design dimensions for the test cavity arrays.

To ensure that our characterization is independent along both the *x*- and *y*-axes, the cavity array in Fig. 5(a) is positioned such that Cavity #5 is at the origin of the *x-y* plane (center of the LCD), as illustrated in Fig. 5(c) and 5(d), respectively. With the X-Axis test print, the center of Cavity #5 is offset from the origin by +50 μm along the *x*-axis (no offset on the *y*-axis). With the Y-Axis test print, the center of Cavity #5 is offset from the origin by -50 μm along the *y*-axis (no offset on the *x*-axis).
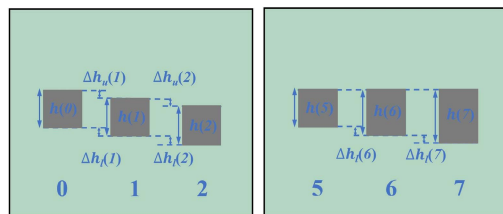
Photographs of the 3-D printed cavity arrays for the *x*- and *y*-axes are shown in Fig. 6(a) and 6(b), respectively. It can be seen that corner rounding print defects exist,

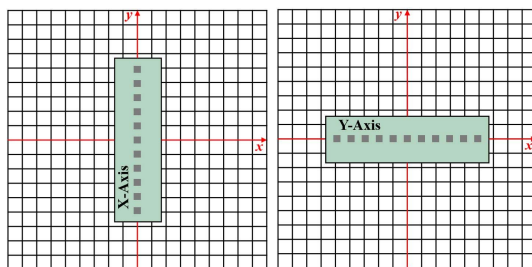**TABLE 8.** CAD target design dimensions for cavity arrays.

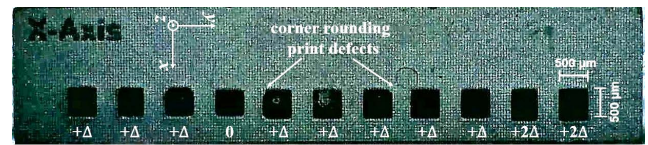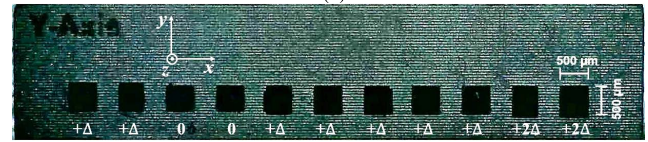| Cavity #	Dimensions (μm)		
i	$h(i)$	$\Delta h_u(i)$	$\Delta h_l(i)$
0	500	0	0
1	500	+10	+10
2	500	+10	+10
3	500	+10	+10
4	500	+10	+10
5	500	+10	+10
6	510	0	+10
7	520	0	+10
8	530	0	+10
9	540	0	+10
10	550	0	+10
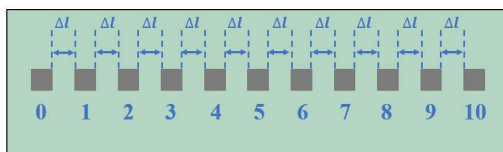
FIGURE 5. Cavity array designs for characterizing dimensional quantization: (a) overview; (b) close-in views; (c) X-Axis test print orientation; and (d) Y-Axis test print orientation.

FIGURE 6. 3-D printed cavity arrays for characterizing dimensional quantization: (a) microphotograph of the X-Axis test print; (b) microphotograph of the Y-Axis test print; (c) measured cavity height; and (d) measured boundary offset. The pixel pitch corresponds to the minimum feature size and quantization level of $\Delta = 50\,\mu$m.
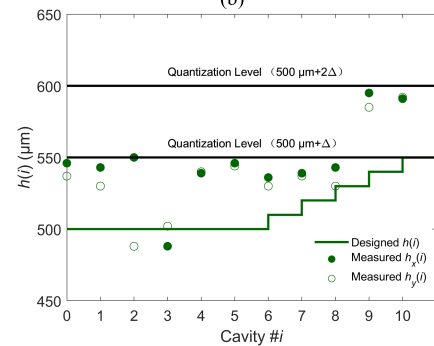
due to increasing quality degradation with printer usage. In Appendix B, Table B1 gives the measured dimensions for all the cavities shown in Fig. 6(a) and 6(b) and these are plotted in Fig. 6(c) and 6(d). It can be seen for $h(i)$ in Fig. 6(c), after the relatively large random errors (within $\pm 31\,\mu$m) are taken into account, there are step changes in dimensions (e.g., between Cavities #2 and #3, #3 and #4, #8 and #9) with the X-Axis test print; while similar quantization step changes (e.g., between Cavities #1 and #2, #3 and #4, #8 and #9) are seen with the Y-Axis test print. For the boundary offset $\Delta h(i)$ in Fig. 6(d), after the smaller random errors (within -14 μm and +17 μm) are taken into account, there are six clear quantization step changes associated with the X-Axis and Y-Axis test print dimensions.

It can be concluded that: (i) random errors are relatively large (combination of printing and measurement); (ii) $\pm 50\,\mu$m quantization is observed with our test prints; (iii) vertical offsets with Cavities #1 to #5 and height changes in Cavities #6 to #10 experience systematic (quantization) errors.

Ideally, the printed dimensions are discretized by the number of pixels. In practice, some cases can extend to the next quantization level, as shown in Fig. 7. This is based on the assumption that four printing decision thresholds are located at the boundaries of the pixel. Figure 7(a) shows the ideal case, where the target cavity boundary and the resulting printing boundary overlap (i.e., no registration errors). Figure 7(b) and 7(c) represent scenarios where quantization errors are observed in the printing, due to a registration error along the x- and y- axes, respectively. Figure 7(d) illustrates pixel
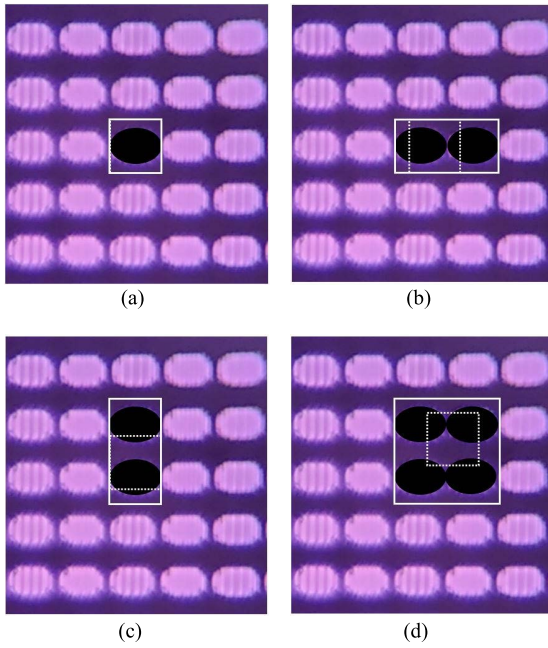
FIGURE 7. Illustrations of pixel quantization for a single pixel cavity within a 5 × 5 sub-array of LCD pixels: (a) with no registration error; (b) registration error along the x-axis; (c) registration error along the y-axis; and (d) registration errors along the x- and y-axes. Dotted white square box indicates the target cavity boundaries defined in the original CAD drawing software; while the solid white rectangle indicates the resulting pixels assigned by the printer's slicing software, due to registration error.
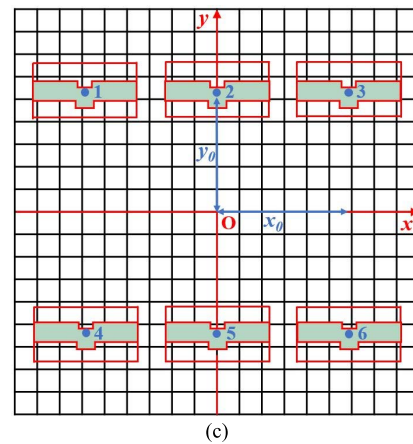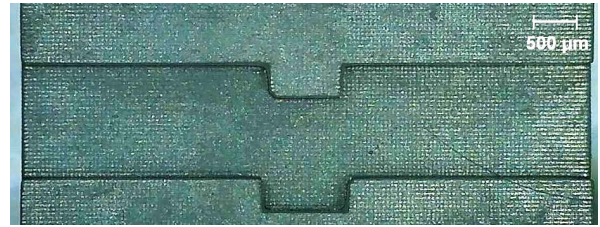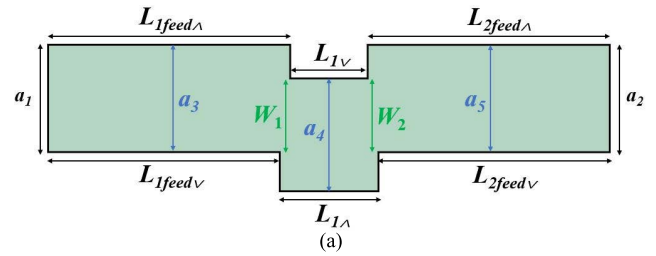

FIGURE 8. Batch printing of transverse offset single cavities for characterizing dimensional quantization: (a) target design of a single part in CAD drawing; (b) photograph of a single part; and (c) spatial orientation and even distribution for six parts in slicing software.

quantization due to registration errors along both the *x*- and *y*-axes.

Now, multiple parts can be 3-D printed at the same time, to improve throughput efficiency and to slow-down print quality degradation with usage. However, the location of the printed part will dictate its final dimensions; with its relative sensitivity increasing as its minimum feature size decreases. For this reason, the second type of test print is investigated for their physical dimensions with the batch processing of six parts in one print run. Figure 8(a) shows the target design of a transverse offset single cavity part and Fig. 8(b) shows the corresponding photograph. Figure 8(c) illustrates the spatial orientation and even distributions for a batch print of six parts; identified as Parts #1 to #6. The center of each part is separated from the adjacent part by $x_0 = 10.00$ mm in the *x*-direction and $2y_0 = 37.50$ mm in the *y*-direction.

The target design and resulting measured physical dimensions for six parts are given in Table B2. Note that the design dimensions have 50 μm metal plating thickness compensation (to replicate the realistic scenario for our final filters; thinner layers may not guarantee corner plating).

From our measurements, it has been found that if perfect symmetry about the *x*- and/or *y*-axes is established, in both the CAD drawing and slicing software, then the symmetry of the printed physical dimensions along the respective *y*- and/or *x*-directions is also preserved. For example, with respect to Fig. 8, with the parts centered on the *y*-axis, $L_{1feed\wedge}(2) \cong$

$L_{2feed\wedge}(2)$, $L_{1feed\vee}(2) \cong L_{2feed\vee}(2)$ and $L_{1feed\wedge}(5) \cong L_{2feed\wedge}(5)$, $L_{1feed\vee}(5) \cong L_{2feed\vee}(5)$). As another example, with Parts #1 and #3, $L_{1feed\vee}(1) \cong L_{2feed\vee}(3)$, $L_{2feed\vee}(1) \cong L_{1feed\vee}(3)$ and $L_{1\vee}(1) \cong L_{1\vee}(3)$. Conversely, where there is no symmetry, there can be a difference of $\Delta = 50\,\mu$m; for example, with $L_{1feed\wedge}(1)$ and $L_{2feed\wedge}(1)$. As a result, our findings predict that quantization can create a significant asymmetry in cavity lengths with our symmetrical (about the *y*-axis) 5th order G-band filter.

In addition, we have found that with part features that have boundaries running parallel to the *x*- or *y*-axes, the printed physical dimensions along the respective *y*- or *x*-directions is also preserved. For example, with Parts #1 to #3, $a_4(1) \cong a_4(2) \cong a_4(3)$, since the pair of lines connecting their common feature are running parallel to the *x*-axis. As another example, with Parts #1 and #4, $L_{1feed\wedge}(1) \cong L_{1feed\wedge}(4)$, since the pair of lines connecting their common feature are running parallel to the *y*-axis. Conversely, where a pair of parallel lines are offset, there can be a difference of $\Delta = 50\,\mu$m; for example with $a_3(6) \cong a_5(6)$ and $a_4(6)$. As a
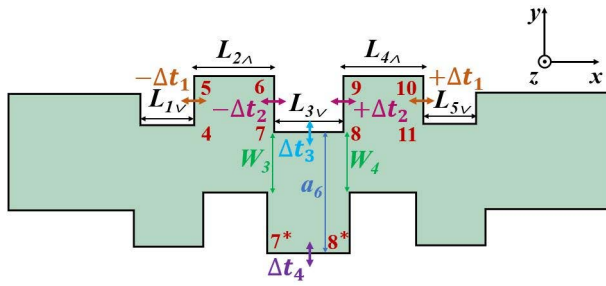
FIGURE 9. Monte-Carlo analysis with four boundary scenarios.

result, our findings predict that quantization associated with MSLA printers can create a significant step-change in the cavity widths along the length of our G-band transverse offset filter.

B. MONTE-CARLO ANALYSIS

Monte-Carlo analysis is a useful technique for investigating filter performance sensitivity to quantization errors. One CFF and one Chebyshev filter are manufactured in separate print runs; the center points of both filters (in the x-y plane) are positioned at the same location along the y-axis. The resulting symmetry is then exploited to facilitate a more sparse Monte-Carlo analysis, to avoid the heavy computational resources needed when applying global analysis for every possible dimensional variation. Four representative boundary (B) scenarios are investigated, each with a possible variation of $\Delta t_i = \pm \Delta$ (associated with boundary scenario $i \in [1, 2, 3, 4]$). With reference to Fig. 9, with $i = 1$, $B_{4\text{-}5} \leftrightarrow B_{10\text{-}11}$ represents a boundary pair resulting in locked cavity lengths $L_{1\vee} = L_{5\vee}$ and $L_{2\vee} = L_{4\vee}$. Similarly, with $i = 2$, $B_{6\text{-}7} \leftrightarrow B_{8\text{-}9}$ represents a boundary pair with locked cavity length $L_{2\wedge} = L_{4\wedge}$. Finally, with $i = 3$ and 4, the respective $B_{7\text{-}8}$ and $B_{7^*\text{-}8^*}$ boundaries are independent of each other; with both resulting in a variation in a_6, while $W_3 = W_4$ is only dependent on $B_{7\text{-}8}$.

Figure 10 shows the frequency responses for our non-predistorted $\{1, 1, 1, 2\}$ chained-function filter, with quantized variations in the four boundary scenarios. It can be seen that variations with Δt_1 and Δt_2 introduce similar levels of frequency detuning. Also, the filter is most sensitive to variations in Δt_3, which result in errors associated with both the iris gap widths $W_3 = W_4$ and the cavity width a_6. With the former, variations in Δt_3 has significant effects on the filter's bandwidth, with over-coupling when $\Delta t_3 = +\Delta$ and under-coupling when $\Delta t_3 = -\Delta$. The filter is least sensitive to variations in Δt_4, which only introduce errors on the cavity width a_6. From these simulation results, our non-pre-distorted G-band filter fails to meet its target specifications with the first three scenarios, while the last scenario demonstrates some resilience to its quantized boundary variations. Obviously, a practical scenario would have to superimpose the effects from all possible boundary scenarios and, therefore,
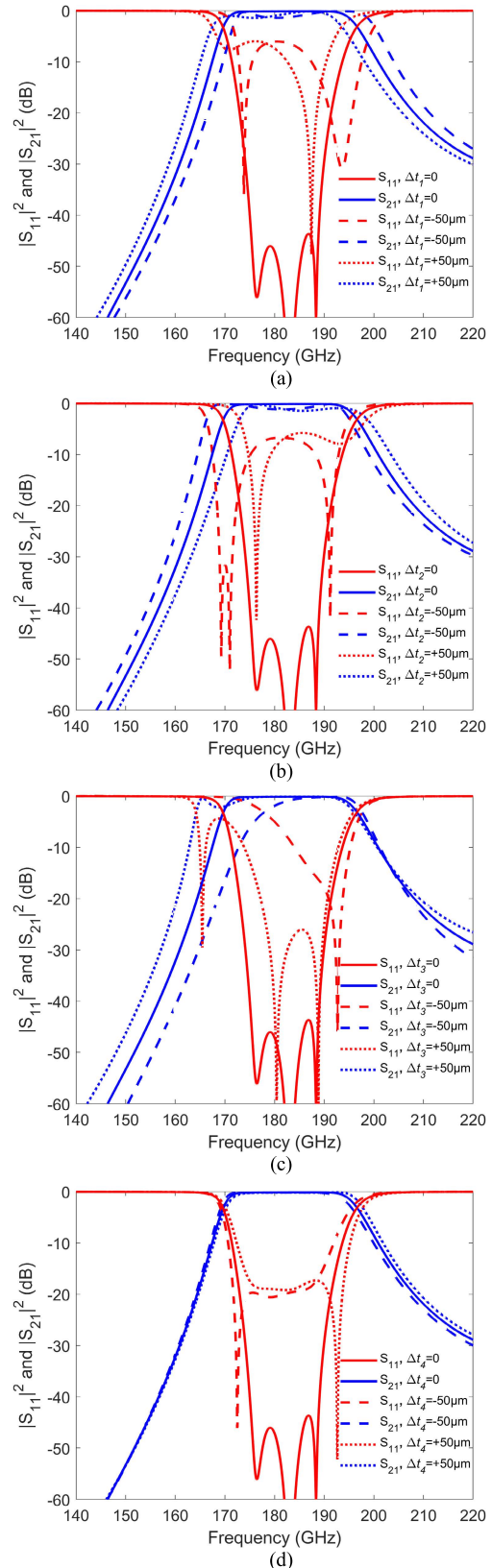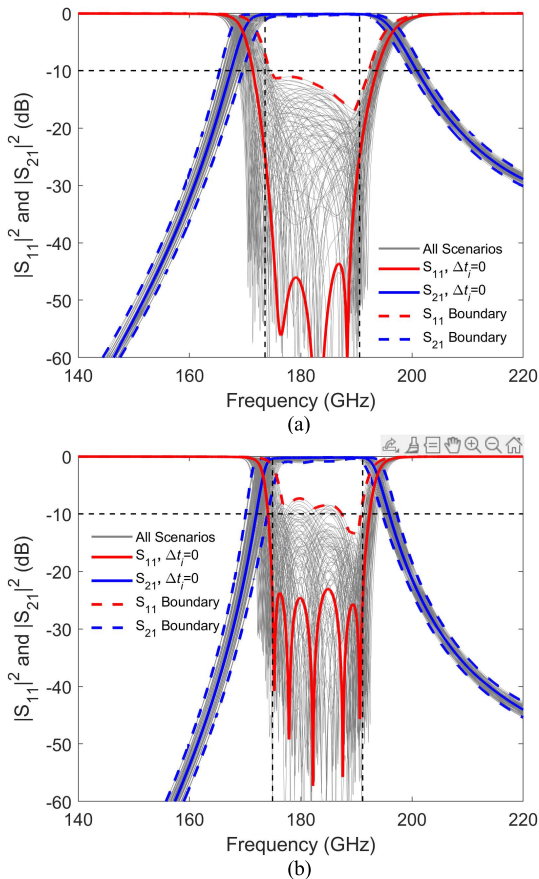

FIGURE 10. Simulated results for a non-pre-distorted 5th order G-band $\{1, 1, 1, 2\}$ chained-function filter with four boundary scenarios having variations of $\mu \Delta t_i = \pm 50$ μm: (a) $i = 1$; (b) $i = 2$; (c) $i = 3$; and (d) $i = 4$.
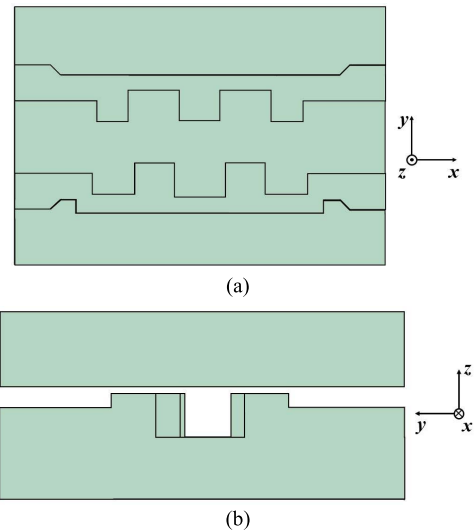
FIGURE 11. Monte-Carlo simulation results for non-pre-distorted 5th order G-band filters with four boundary scenarios having variations of $\mu \Delta t_i = \pm 10 \mu m$: (a) $\{1, 1, 1, 2\}$ CFF; and (b) Chebyshev filter. The vertical black dashed lines indicate the 25 dB return loss target design bandwidth, while the horizontal black dashed lines indicates the acceptable level of measured passband return loss.

FIGURE 12. CAD drawings for our 3-D printed H-plane split-block transverse offset inductive iris G-band 5th order $\{1, 1, 1, 2\}$ chained-function MPRWG filter (having 50 μm metal plating thickness compensation): (a) plan view of the bottom part; and (b) end view showing both parts.
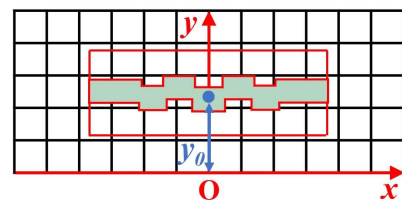
FIGURE 13. Position and orientation of the bottom part of the 3-D printed H-plane split-block transverse offset inductive iris G-band 5th order MPRWG filters (having 50 μm metal plating thickness compensation) in slicing software.

unless there is (near-)perfect registration then the filter will always fail.

Having demonstrated that the non-pre-distorted CFF fails with 50 μm quantized variations, the same is also found with Chebyshev filters. However, with the continual advances being made with affordable higher resolution MSLA printers, it is appropriate to investigate the resilience of future CFFs and Chebyshev filters using Monte-Carlo analysis with $\Delta = 10 \mu m$. To this end, Fig. 11(a) and 11(b) compare the frequency responses for our two filters, having all possible combinations (i.e., $3^4 = 81$) of Δt_i; the solid lines correspond to the target design filter responses (i.e., with $\Delta t_i = 0$), the grey lines represent all possible combinations and the dash lines represent extreme boundaries. It is found that the in-band return loss levels for the CFF and Chebyshev filter are generally better than 11.1 dB and 7.3 dB, respectively. Clearly, the CFF is less sensitive to quantization errors, when compared to the Chebyshev filter.

C. MULTI-STEP QUANTIZATION PREDISTORTION

For the first time, we introduce a multi-step quantization pre-distortion methodology that can be applied to 3-D printing.

Here, the registration errors (all being within $\pm \Delta$) associated with boundaries are corrected for in subsequent design iterations; each step addresses different boundaries, until all boundaries have been corrected.

Figure 12 shows CAD drawings for our 3-D printed H-plane split-block transverse offset G-band 5th order $\{1, 1, 1, 2\}$ chained-function filter (having 50 μm metal plating thickness compensation). As illustrated in Fig. 13, and mentioned previously, the center points of the CFF and Chebyshev filters are positioned along the y-axis (with an arbitrary separation of $y_0 = 18.75$ mm from the x-axis).

It should be noted that, in order to compare the manufacturing sensitivity of both filters, predistortion can keep both filters under similar levels of physical dimensional error. Conversely, without predistortion, both filters could suffer from different levels of dimensional errors and, therefore, their manufacturing sensitivities cannot be compared. For this reason, we will not consider the non-pre-distorted Chebyshev filter.

Figure 14 illustrates four-step quantization predistortion applied to the boundaries for a 5th order transverse offset
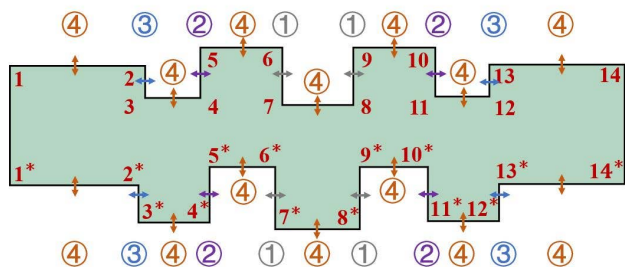
FIGURE 14. Four-step quantization predistortion for the transverse offset inductive iris 5th order MPRWG filter. The number within the circle and the associated color coding represent the iteration step number.

inductive iris waveguide filter. Starting at the center of the filter, the first three steps (grey, purple and then blue) address boundaries associated with defining cavity lengths; while the last step (brown) addresses boundaries associated with defining cavity widths (a_1 to a_9) and iris gap widths (W_1 to W_6).

With iteration Step 1, predistortion will change the lengths associated with the center cavity (L_3) and this will also change the lengths of the two adjacent cavities (L_2 and L_4); this needs correcting in iteration Step 2. A cascading effect to the outer two adjacent cavities (L_1 and L_5) needs correction in iteration Step 3. Since boundaries that are associated with the width of the waveguide do not have cascading effects, their predistortion can be realized simultaneously in Step 4. For the same reason, predistortion to the waveguide height ($b_1 = b_2$) can also be applied in this last step.

An example of our multi-step quantization predistortion methodology will now be given for our chained-function filter. With reference to Fig. 15, the black lines represent design boundaries with the previous iteration; while the blue lines show the predistortion design boundaries for the current iteration. The predistortion introduced in iteration Step i is represented by Δp_i ($i \in [1, 2, 3]$), where $\Delta p_i < \Delta$.

Our non-pre-distorted chained-function filter, with the original target design dimensions (having 50 μm metal plating thickness compensation) is printed as a reference for the predistortion in iteration Step 1.

With reference to the measured dimensions without predistortion, given in Table B3, the measured center cavity length $L_{3\wedge}$ (for the original non-pre-distorted filter) is found to be reduced by *ca.* 120 μm. For Step 1, the positions of the $B_{6*-7*} \leftrightarrow B_{8*-9*}$ boundary pair should be corrected for by Δp_1 at each boundary, due to symmetry. As a result, the designed dimension for the center cavity length $L_{3\wedge}$ is increased by $2\Delta p_1$, where our predistortion value is chosen here to be $\Delta p_1 = \Delta/2$; leading to a measured cavity length increase of approximately $+2\Delta$. To maintain a fixed total filter length, the designed input and output inner feed lengths must be reduced by both $\Delta/2$, as shown in Fig. 15(a).

The filter with the pre-distorted dimensions in Step 1 is printed as a new reference, for predistortion in Step 2. With
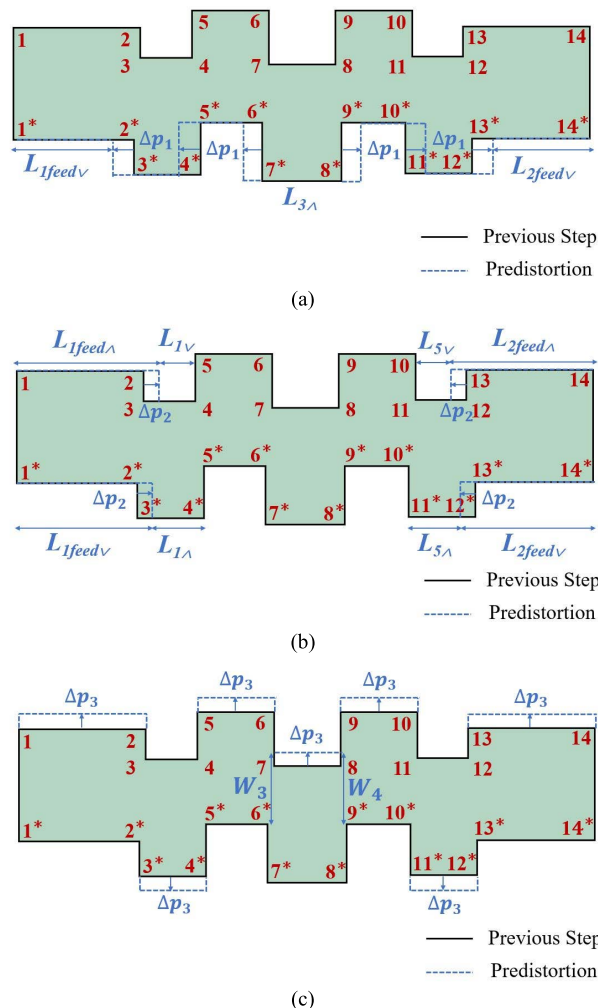
FIGURE 15. Three-step quantization predistortion for our 5th order transverse offset inductive iris waveguide CFF: (a) Step 1; (b) Step 2; and (c) Step 3.

reference to the measured dimensions with predistortion in Step 1, given in Table B3, it is found that there are no registration errors for $L_{2\wedge}, L_{2\vee}, L_{4\wedge}, L_{4\vee}$. Therefore, predistortion is not needed for these dimensions, and the next boundaries can be considered. The positions of the $B_{2-3} \leftrightarrow B_{12-13}$ and $B_{2*-3*} \leftrightarrow B_{12*-13*}$ boundary pairs should be corrected for by Δp_2, due to symmetry. As a result, the designed dimensions for the associated cavity lengths $L_{1\wedge}, L_{1\vee}, L_{5\wedge}, L_{5\vee}$ are all decreased by Δp_2, where our predistortion value is again chosen here to be $\Delta p_2 = \Delta/2$; leading to a measured cavity length decrease of approximately Δ.

The filter with the pre-distorted dimensions in Step 2 is printed as a new reference, for predistortion in Step 3. With reference to the measured dimensions with predistortion in Step 2, given in Table B3, after characterizing the registration error, predistortion can now be introduced to Step 3. Here, all measured cavity widths are reduced by ~45 μm and the measured iris gap widths W_3 and W_4 are reduced
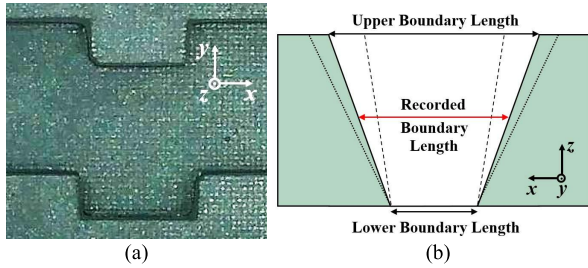
FIGURE 16. Internal sidewall boundaries for the bottom part of a cavity waveguide filter: (a) microphotograph of the plan view; and (b) exaggerated side-view illustration for measuring boundaries. The dashed lines approximate the sidewalls for a new printer. Dotted lines show the increased slope of the sidewalls with overused printer.

FIGURE 17. Microphotographs for the bottom parts of our 3-D printed fully pre-distorted filters (before plating): (a) chained-function filter; and (b) Chebyshev filter. The red rectangles represent the recorded boundaries.

by $\sim$40 μm; with the other iris gap widths being approximately correct, when compared to the target design values. Therefore, an error compensation of $\Delta p_3 = 30\,\mu$m is applied, as illustrated in Fig. 15(c). Finally, a compensation of $+20$ μm is applied to $b_1 = b_2$, for waveguide height predistortion.

Dimension measurements for our chained-function and Chebyshev filters, for exact iterative step are given in Tables B3 and B4, respectively. To simplify the predistortion procedures for the Chebyshev filters, all port dimensions have already been pre-distorted, based on Step 3 with our previous chained-function filters.

With dimension measurements, it is found that all the internal sidewalls are non-vertical; creating two x-y boundary lengths (upper and lower), shown in Fig. 16(a) and with an exaggerated side-view illustration in Fig. 16(b). The recorded boundary dimensions represent the arithmetic mean values from the measured upper and lower boundary lengths. For example, the bottom parts for our 3-D printed fully pre-distorted filters (before plating) are shown in Fig. 17, with the red rectangles representing the recorded boundary dimensions.

Using our multi-step quantization predistortion methodology, we have now removed the identified systematic (quantization) errors in the 3-D printed parts; leaving behind only the random errors (within $\pm31\,\mu$m), if age-related drifting errors are ignored.

VI. FABRICATION
A. 3-D PRINTING WITH POST PROCESSING
With our MSLA printer, the Elegoo water washable photopolymer resin (Ceramic Grey) was employed; mainly for its high precision, low shrinkage, ease of post-processing and low odor. After 3-D printing, samples are post-processed with the following room temperature sequence [5]: (i) remove parts from the printer's build platform; (ii) pre-rinse parts in a container of water; (iii) mechanically remove support materials; (iv) clean parts using a water jet; (v) use ultrasonic cleaning for 2 minutes; (vi) dry parts with compressed air; (vii) cure parts with a weak UV light source for 10 minutes;
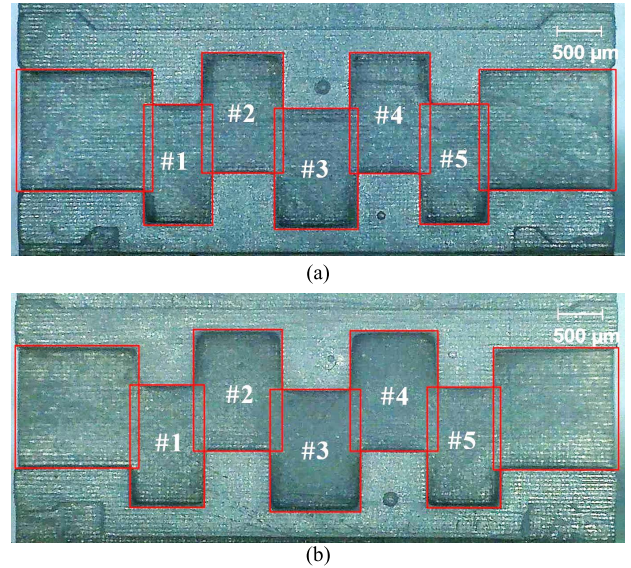
and (viii) fully-cure by placing parts under natural light for a number of hours.

B. METALIZATION
After visual inspection (rejecting those with significant manufacturing defects), the fully pre-distorted filters are metal plated using a commercial process. After cleaning, a thin layer of nickel is deposited (using electroless plating), followed by a 50 μm thick layer of copper (electroplated); finally, the plated parts undergo an anti-tarnishing treatment. A complete H-plane split-block chained-function filter is shown in Fig. 18.

VII. MEASUREMENTS
Scattering (S-)parameter measurements were conducted within the Department of Electromagnetic and Electrochemical Technologies at the U.K.'s National Physical Laboratory (NPL), using their Keysight Technologies PNA-X N5247B vector network analyzer – with VDI WR-5.1 frequency extension heads [43]. The measurement setup for the 3-D printed filters is shown in Fig. 19. The filter under test is placed between two test flanges; four stainless steel dowel pins and four stainless steel M2 screws (each with a pair of washers and a nut), running through both test port flanges and the assembled filter, are respectively used for alignment and ensuring a tight fit.

A. NON-PRE-DISTORTED CHAINED-FUNCTION FILTER
Figure 20 shows a microphotograph of the bottom part of the non-pre-distorted chained-function filter (after plating) and its recorded boundaries. The measured physical dimensions are given in Table B5. It can be clearly seen from the

(a)

(b)
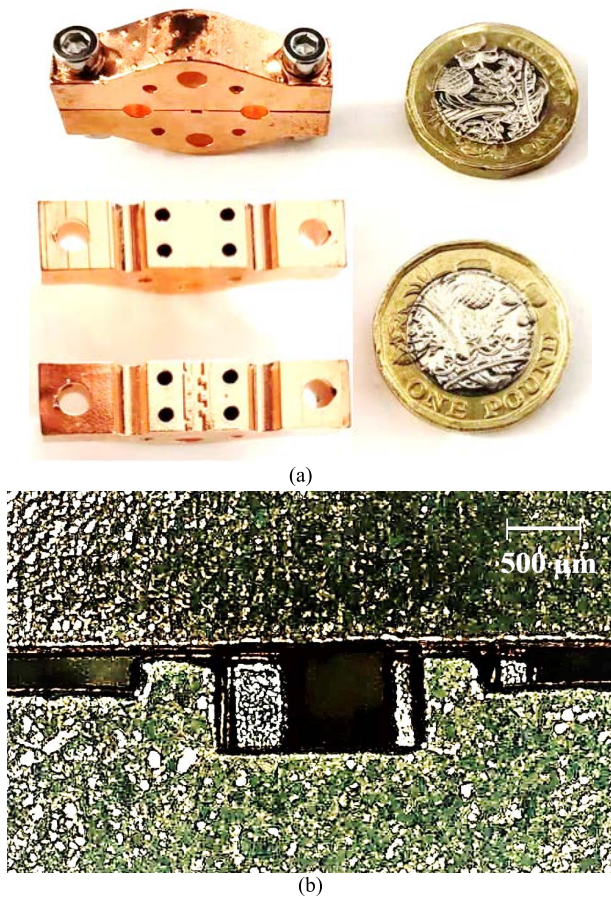
FIGURE 18. 3-D printed H-plane split-block G-band 5th order CFF (after plating): (a) photographs of assembled (top) and disassembled (bottom) filter with British pound coin to indicate scale; (b) microphotograph of one of the ports.
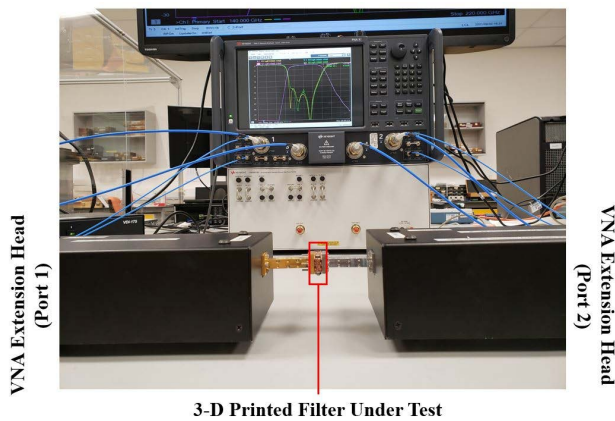
FIGURE 19. Measurement setup for the 3-D printed G-band filters.

overlapping red boxes, in Fig. 20, that there are significant misalignments between Cavities #1 ↔ #2 and Cavities #4 ↔ #5, which is caused by quantization errors. In addition, a 260 μm diameter circular shallow pit can be seen inside Cavity #4; believed to have been introduced during the electroplating process. From simulations, with a 15 μm deep pit

FIGURE 20. Microphotograph of the bottom part of our non-pre-distorted G-band 5th order chained-function filter (after plating). The red rectangles represent the recorded boundary dimensions.
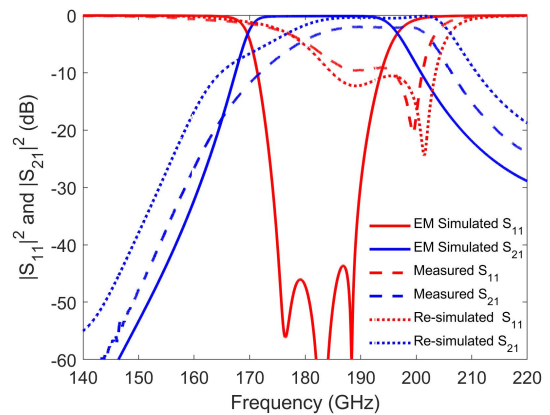
FIGURE 21. EM simulated, measured and re-simulated S-parameter responses for the non-pre-distorted G-band 5th order chained-function filter.

defect, it was found that insertion loss degrades by less than 0.01 dB.

Corner rounding of the cavities (in the *x-y* plane) increases all the coupling coefficients and, therefore, the filter's bandwidth. As a result, circular corner rounding is considered in the re-simulations (given the measured dimensions of the plated filter in Table B5). The average corner rounding radius is 82 μm for this filter. The simulated, measured and re-simulated S-parameter responses for our non-pre-distorted chained-function filter are given in Fig. 21.

The measured passband insertion loss is 2.0 dB at its new center frequency of 190.5 GHz (i.e., 3.9% frequency up-shifted from 183.3 GHz). Since copper is used in the re-simulations, giving a passband insertion loss of only 0.4 dB, the higher measured loss is believed to be attributed to radiation leakage from tiny gaps between the upper and lower parts of the split block assembly. The measured and re-simulated return losses are in good agreement, which indicates the accuracy of the measured dimensions. The frequency shift and poor return loss are mainly due to cavity length $L_{3\wedge}$ shrinking by 2Δ and all cavity widths a_i ($i \in [1, 2, \ldots, 9]$) shrinking by Δ. This clearly shows the sensitivity of G-band 5th order MPRWG filters to systematic (quantization) errors. Indeed, with our MSLA printer, $\Delta = 50$ μm corresponds to the MPRWG having respective electrical lengths of 4.7°, 8.3° and 11.2° at 140, 180 and 220 GHz. Therefore, with a half-wavelength cavity resonator, ideally tuned to 183.3 GHz,

FIGURE 22. Microphotograph of the bottom part of our fully pre-distorted G-band 5th order Chebyshev filter (after plating). The red rectangles represent the recorded boundary dimensions.

FIGURE 23. EM simulated, measured and re-simulated S-parameter responses for the pre-distorted G-band 5th order Chebyshev filter.

FIGURE 24. Microphotograph of the bottom part of our fully pre-distorted G-band 5th order chained-function filter (after plating). The red rectangles represent the recorded boundary dimensions.

FIGURE 25. EM simulated, measured and re-simulated S-parameter responses for the pre-distorted G-band 5th order chained-function filter.

an $8.5°$ change in electrical length (due to a reduction in cavity length by Δ) corresponds to a 3.5% frequency up-shift. For this reason, predistortion is required to mitigate against the systematic errors caused by 3-D printing quantization.

B. PRE-DISTORTED CHEBYSHEV FILTER

Figure 22 shows a microphotograph of the fully pre-distorted Chebyshev filter (after plating) and its recorded boundaries. The measured physical dimensions are given in Table B6. As expected, any overlap of the red boxes is due to random errors that are less than the quantization error. The average corner rounding radius is 87 μm for this filter, which is consistent with the previous filter.

The simulated, measured and re-simulated S-parameter responses for our pre-distorted Chebyshev filter are given in Fig. 23. The measured passband insertion loss is 0.6 dB at its new center frequency of 177.3 GHz (i.e., 3.3% frequency down-shifted from 183.3 GHz). Our re-simulated insertion loss of 0.2 dB suggests a lower level of radiation leakage; with the modeling discrepancy of only 0.4 dB being mainly attributed to surface roughness. The poor return loss performance clearly shows the sensitivity to manufacturing errors with Chebyshev filters, even when predistortion is applied. Finally, the measured and re-simulated responses are all in good agreement.

C. PRE-DISTORTED CHAINED-FUNCTION FILTER

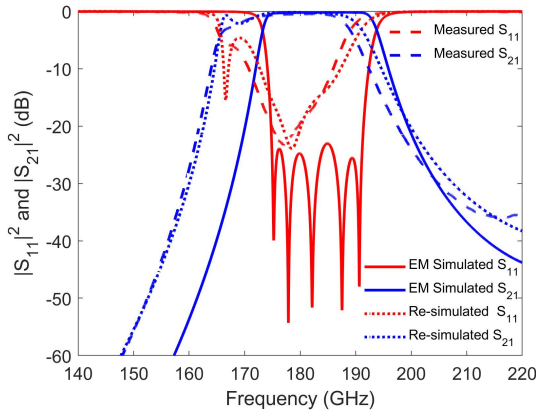Figure 24 shows a microphotograph of the pre-distorted chained-function filter (after plating) and its recorded

boundaries. The measured physical dimensions are given in Table B7. As with the pre-distorted Chebyshev filter, any overlap of the red boxes is due to random errors that are less than the quantization error. The average corner rounding radius is 85 μm for this filter, which is consistent with the previous two filters. Similar to its non-pre-distorted counterpart, three 300 μm diameter circular shallow pits can be seen inside Cavities #1, #3 and #5; again, these are believed to have been introduced during the electroplating process.

The simulated, measured and re-simulated S-parameter responses for our pre-distorted CFF are given in Fig. 25. The measured passband insertion loss is again 0.6 dB at its new center frequency of 181.7 GHz (i.e., 0.9% frequency down-shifted from 183.3 GHz). The discrepancy between the simulated and measured responses is due to the large pixel size and corner rounding. Our re-simulated insertion loss is again 0.2 dB and so this supports our assumptions of low radiation leakage and the modeling discrepancy being mainly attributed to surface roughness.

The return loss performance clearly shows some sensitivity to manufacturing errors with our pre-distorted CFF. However, the measured return loss is now acceptable, being better than 13 dB across the whole passband. Finally, the measured and re-simulated responses are all in good agreement.

Comparing our pre-distorted Chebyshev and chained-function filters, having similar measured levels of dimensional errors (seen in Tables B6 and B7, respectively), the latter clearly shows a lower sensitivity to manufacturing errors.

VIII. CONCLUSION

With both subtractive and additive manufacturing, the ability to accurately define critical internal features gets harder as the frequency and filter order increase. From a comprehensive literature survey of metal waveguide bandpass filters, only 11 commercial-off-the-shelf products could be found online having a lower-passband cut-off frequency above 110 GHz; all realized using subtractive manufacturing technologies. Moreover, using additive manufacturing, only 13 millimeter-wave 3-D printed metal waveguide bandpass filters could be found online; there are only 3 above 110 GHz, all realized using metal-based MLS 3-D printing technology.

This clearly highlights the importance for new research to mitigate against manufacturing errors, especially for applications above 110 GHz. To this end, we have identified, characterized and proposed a design methodology to address systematic (quantization) errors associated with pixel-based 3-D printing.

Having a reduced sensitivity to manufacturing errors, a G-band 5th order chained-function filter has been demonstrated, with a prescribed center frequency of 183.3 GHz, worst-case return loss level of 25 dB and corresponding fractional bandwidth of 9.3%. A corresponding Chebyshev filter with the same specifications was designed as a reference. Employing more conventional inductive diaphragm irises, between cavity resonators, at this frequency, can be challenging with additive manufacturing; depending on the technologies used, they can be very brittle and easily damaged when 3-D printing and/or during subsequent post processing and metal plating. For this reason, we adopted the more robust transverse offset inductive irises.

For our work, a low-cost MSLA 3-D printer was chosen, having a pixel pitch that has an equivalent electrical length of 8.5° at center frequency. In order to characterize the quantization effects in the *x*-*y* plane of the build platform, two different types of cavity test prints were investigated for their physical dimensions. With the former, it is found that changes in part location and/or design size result in quantization errors. With the latter, if perfect symmetry about the *x*- and/or *y*-axes is established, in both the CAD drawing and slicing software, then the symmetry of the printed physical dimensions along the respective *y*- and/or *x*-directions is also preserved. In addition, with features that have boundaries running parallel to the *x*- or *y*-axes, the printed physical dimensions along the respective *y*- or *x*-directions is also preserved. Therefore, the center points for all our filters were positioned along the *y*-axis, in order to maintain symmetry in the filter cavity lengths.

Based on the discretization properties associated with our MSLA 3-D printer, a multi-step quantization predistortion methodology was introduced for the first time to correct for registration errors.

Two chained-function filters (with and without predistortion) and one Chebyshev filter (with predistortion) were printed, plated and measured. As expected, the robust

pre-distorted chained-function filter demonstrated a low insertion loss of only 0.6 dB at its center frequency of 181.7 GHz, having a 0.9% frequency shift, and an acceptable worst-case passband return loss of 13 dB. Moreover, with measured dimensions after the 3-D printed parts have been commercially electroplated with a 50 μm thick layer of copper, the re-simulations are in good agreement with the S-parameter measurements.

When compared to the non-pre-distorted case, this confirms that quantization predistortion improves print accuracy by removing this systematic error and, thus, provides a better filter performance. As expected, the CFF demonstrates a lower sensitivity to manufacturing errors, when compared to the Chebyshev filter.

For the first time, quantization errors associated with a pixel-based 3-D printer have been characterized and our robust predistortion methodology has been successfully demonstrated with an upper-millimeter-wave circuit. Indeed, we report the first polymer-based 3-D printed filters that operate above W-band.

As pixel sizes continue to shrink, (sub-)THz filters with ever-higher frequencies of operation and more demanding specifications can be manufactured. Moreover, our work opens-up new opportunities for any pixel-based technology, which exhibits registration errors, with its application critically dependent on its minimum feature size.

APPENDIX A

For a rectangular waveguide bandpass filter, the general transfer function is given as [44]:

$$|S_{21}(j\omega)|^2 = \frac{1}{1 + \varepsilon_T^2 \psi_N^2 \left[\alpha_1 \left(\frac{\lambda_g}{\lambda_{g0}} \right) \sin \left(\pi \frac{\lambda_{g0}}{\lambda_g} \right) \right]} \quad \text{(A1)}$$

where, ε_T ($0 < \varepsilon \leq 1$) defines the worst-case passband return loss level; ψ_N is an Nth order filter polynomial function; $\alpha_1 = \left[(\lambda_{g1}/\lambda_{g0}) \sin (\pi \lambda_{g0}/\lambda_{g1}) \right]^{-1}$ is the lowpass-to-bandpass scaling factor for a waveguide filter; λ_g is the guided wavelength; $\lambda_{g0} \approx (\lambda_{g1} + \lambda_{g2})/2$ is the center frequency guided wavelength, where λ_{g1} and λ_{g2} correspond to guided wavelengths of the upper and lower band-edge frequencies, respectively.

Consider a passive two-port symmetrical and reciprocal lossless filter, the voltage-wave reflection coefficient at the input port $S_{11}(s)$ can be related to two finite-degree polynomials $E(s)$ and $F(s)$ as follows:

$$S_{11}(s) = S_{22}(s) = \frac{F(s)}{\varepsilon_R E(s)} \quad \text{(A2)}$$

where, $s = j\omega$ is the complex frequency for the steady state. With a filter network: $E(s)$ is an Nth order polynomial having complex coefficients $e_0, e_1, e_2, \ldots, e_N$; $F(s)$ is an Nth order polynomial having complex coefficients $f_0, f_1, f_2, \ldots, f_N$; ε_R is a real-valued scaling constant, such that $|S_{11}(s)| \leq 1$.

Similarly, the voltage-wave transmission coefficients $S_{21}(s)$ and $S_{21}(s)$ are given by:

$$S_{21}(s) = S_{12}(s) = \frac{P(s)}{\varepsilon_T E(s)} \qquad \text{(A3)}$$

where, ε_T is a real-valued scaling constant, such that $|S_{21}(s)| \leq 1$. $P(s)$ is related to polynomials $E(s)$ and $F(s)$, through the conservation of energy principle, by the following:

$$\frac{P(s)P(s)^*}{\varepsilon_T^2} = E(s)E(s)^* - \frac{F(s)F(s)^*}{\varepsilon_R^2} \qquad \text{(A4)}$$

With a short circuit at either the input or output port, the normalized admittance polynomial $y_{22}(s)$ or $y_{21}(s)$, respectively, are related to reflection and transmission polynomials as follows:

$$y_{22}(s) = \frac{y_{22n}(s)}{y_d(s)} = \frac{n_1(s)}{m_1(s)} \quad \text{for even } N \qquad \text{(A5)}$$

$$y_{21}(s) = \frac{y_{21n}(s)}{y_d(s)} = \frac{P(s)}{\varepsilon_T m_1(s)} \quad \text{for even } N \qquad \text{(A6)}$$

$$y_{22}(s) = \frac{y_{22n}(s)}{y_d(s)} = \frac{m_1(s)}{n_1(s)} \quad \text{for odd } N \qquad \text{(A7)}$$

$$y_{21}(s) = \frac{y_{21n}(s)}{y_d(s)} = \frac{P(s)}{\varepsilon_T n_1(s)} \quad \text{for odd } N \qquad \text{(A8)}$$

where, $y_d(s)$ are common normalized admittance polynomials that relate to $E(s)$, and the respective polynomials $n_1(s)$ and $m_1(s)$ are given as:

$$\begin{aligned} n_1(s) = &\; j\mathcal{I}m\{e_0 + f_0\} \\ &+ \mathcal{R}e\{e_1 + f_1\}s + j\mathcal{I}m\{e_2 + f_2\}s^2 + \ldots \end{aligned} \qquad \text{(A9)}$$

$$\begin{aligned} m_1(s) = &\; \mathcal{R}e\{e_0 + f_0\} \\ &+ j\mathcal{I}m\{e_1 + f_1\}s + \mathcal{R}e\{e_2 + f_2\}s^2 + \ldots \end{aligned} \qquad \text{(A10)}$$

For a two-port filter, an $N \times N$ coupling matrix M can be formed, representing the mutual couplings between the nodes within the network. With a passive and reciprocal filter, M is real and symmetric about its principal diagonal. Hence, an $N \times N$ orthogonal matrix T exists, giving the following:

$$-M = T \cdot \Lambda \cdot T^t \qquad \text{(A11)}$$

where, $\Lambda = \text{diag}[\lambda_1, \lambda_2, \lambda_3, \ldots, \lambda_N]$ and its elements λ_k (with $k = 1, 2, \ldots, N$) represent eigenvalues of matrix $-M$; and T^t is the transpose of the orthogonal matrix T, giving $T \cdot T^t = I$.

The normalized admittance polynomials can now be expressed as:

$$y_{22}(s) = -j\sum_{k=1}^{N} \frac{T_{Nk}^2}{\omega - \lambda_k} = -j\sum_{k=1}^{N} \frac{r_{22k}}{\omega - \lambda_k} \qquad \text{(A12)}$$

$$y_{21}(s) = -j\sum_{k=1}^{N} \frac{T_{Nk}T_{1k}}{\omega - \lambda_k} = -j\sum_{k=1}^{N} \frac{r_{21k}}{\omega - \lambda_k} \qquad \text{(A13)}$$

where, T_{1k} and T_{Nk} are orthogonal vectors, which respectively correspond to the first and last rows of matrix T.

The residues r_{22k}, r_{21k} and the eigenvalues λ_k can be calculated by using partial fraction expansions [36].

With (A12) and (A13), knowing the residues r_{22k} and r_{21k}, orthogonal vectors T_{1k} and T_{Nk} can be calculated from:

$$T_{Nk} = \sqrt{r_{22k}}, \quad k = 1, 2, \ldots, N \qquad \text{(A14)}$$

$$T_{1k} = \frac{r_{21k}}{T_{Nk}} = \frac{r_{21k}}{\sqrt{r_{22k}}}, \quad k = 1, 2, \ldots, N \qquad \text{(A15)}$$

For a two-port filter, considering its source and load impedances, the direct source-load inverter M_{SL} is:

$$jM_{SL} = y_{21}(s)|_{s \rightarrow j\infty} \qquad \text{(A16)}$$

The final $(N + 2) \times (N + 2)$ prototype coupling matrix M can now be developed [36]. Knowing the coupling elements of M, physical dimensions can be calculated from:

$$K_{S1} = \frac{M_{S1}}{\sqrt{\alpha_2}} \quad \text{and} \quad K_{LN} = \frac{M_{LN}}{\sqrt{\alpha_2}} \qquad \text{(A17)}$$

$$K_{pq} = \frac{M_{pq}}{\alpha_2}, \quad p, q = 1, 2, \ldots, N \qquad \text{(A18)}$$

where, K_{S1} and K_{LN} represent the source-input and output-load coupling coefficients, respectively, and K_{pq} are inter-resonator coupling coefficients. Scaling factor α_2 is given as:

$$\alpha_2 = \frac{(\lambda_{g1} + \lambda_{g2})}{n\pi(\lambda_{g2} - \lambda_{g1})} \qquad \text{(A19)}$$

where, n is the number of half-wavelengths for the waveguide cavity resonator. Consider a conventional 3-cavity cascaded filter, the common-wall couplings between Cavities #1 ↔ #2 and Cavities #2 ↔ #3 have corresponding susceptances B_{12}, B_{23} and the electrical length θ_2 for Cavity #2 is obtained from [36]:

$$B_{12} = K_{12} - \frac{1}{K_{12}} \quad \text{and} \quad B_{23} = K_{23} - \frac{1}{K_{23}} \qquad \text{(A20)}$$

$$\theta_2 = n\pi + \frac{1}{2}\left(\cot^{-1}\frac{B_{12}}{2} + \cot^{-1}\frac{B_{23}}{2}\right) \qquad \text{(A21)}$$

APPENDIX B
See Tables B1–B7.

TABLE B1. Measured physical dimensions for the cavity arrays.

Cavity #	Measured Dimensions (μm)					
i	$h_x(i)$	$\Delta h_{ux}(i)$	$\Delta h_{lx}(i)$	$h_y(i)$	$\Delta h_{uy}(i)$	$\Delta h_{ly}(i)$
0	546	0	0	537	0	0
1	543	+3	0	530	+3	-3
2	550	-10	-3	488	+48	+7
3	488	+55	-7	502	-10	+3
4	539	-3	+48	540	+14	+52
5	546	-3	+3	544	-3	0
6	536	0	-10	530	+14	0
7	539	+3	+7	537	-14	-7
8	543	-14	-10	530	+10	+3
9	595	0	+52	585	-14	+42
10	591	0	-3	592	+10	+17

TABLE B2. Ideally designed and measured physical dimensions for single cavity resonators (compensated for 50 μm plating thickness).

Dimensions (μm)	$L_{1feed\wedge}$	$L_{1feed\vee}$	$L_{1\wedge}$	$L_{1\vee}$	$L_{2feed\wedge}$	$L_{2feed\vee}$	W_1	W_2	a_1	a_2	a_3	a_4	a_5
						Original Design							
	2980	2880	1070	870	2980	2880	1000	1000	1395	1395	1395	1395	1395
Cavity # i						Measured							
1	2984	2882	1046	831	2935	2822	966	969	1352	1355	1359	1356	1359
2	2943	2889	998	886	2930	2872	964	957	1351	1359	1347	1351	1356
3	2934	2832	1043	840	2985	2883	968	971	1355	1349	1351	1353	1353
4	2988	2891	1043	829	2937	2821	1014	1007	1357	1352	1358	1402	1351
5	2949	2903	981	880	2944	2888	1010	1003	1355	1349	1345	1405	1347
6	2935	2840	1041	834	2986	2874	1007	999	1351	1355	1351	1395	1349

TABLE B3. Ideally designed and measured dimensions for pre-distorted chained-function filters (compensated for 50 μm plating thickness).

Dimensions (μm)	$L_{1\wedge}$ / $L_{1feed\wedge}$ / a_1	$L_{1\vee}$ / $L_{1feed\vee}$ / a_2	$L_{2\wedge}$ / $L_{2feed\wedge}$ / a_3	$L_{2\vee}$ / $L_{2feed\vee}$ / a_4	$L_{3\wedge}$ / W_1 / a_5	$L_{3\vee}$ / W_2 / a_6	$L_{4\wedge}$ / W_3 / a_7	$L_{4\vee}$ / W_4 / a_8	$L_{5\wedge}$ / W_5 / a_9	$L_{5\vee}$ / W_6 / b_1	b_2
					Original Design						
	824	624	977	777	1012	812	977	777	824	624	
	1593	1493	1593	1493	1028	824	755	755	824	1028	
	1395	1395	1395	1395	1395	1395	1395	1395	1395	648	648
				Measured with or without Predistortion							
Without Predistortion	849	612	962	736	888	757	951	740	842	627	
	1558	1482	1556	1486	1032	834	744	742	838	1023	
	1355	1347	1349	1347	1354	1356	1351	1351	1345	626	628
Iteration Step 1	857	646	956	747	980	778	950	747	853	648	
	1534	1429	1532	1431	1020	829	730	725	820	1018	
	1343	1353	1350	1350	1350	1354	1350	1339	1352	632	625
Iteration Step 2	801	588	951	735	980	784	942	742	804	588	
	1585	1482	1579	1473	1022	819	716	711	812	1017	
	1351	1348	1356	1347	1354	1347	1354	1345	1354	631	626
Iteration Step 3 (final filter)	793	577	951	738	973	769	947	734	799	570	
	1592	1485	1594	1478	1002	812	751	758	814	1008	
	1409	1411	1417	1411	1404	1409	1411	1409	1409	656	658

TABLE B4. Ideally designed and measured dimensions for pre-distorted Chebyshev filters (compensated for 50 μm plating thickness).

Dimensions (μm)	$L_{1\wedge}$ / $L_{1feed\wedge}$ / a_1	$L_{1\vee}$ / $L_{1feed\vee}$ / a_2	$L_{2\wedge}$ / $L_{2feed\wedge}$ / a_3	$L_{2\vee}$ / $L_{2feed\vee}$ / a_4	$L_{3\wedge}$ / W_1 / a_5	$L_{3\vee}$ / W_2 / a_6	$L_{4\wedge}$ / W_3 / a_7	$L_{4\vee}$ / W_4 / a_8	$L_{5\wedge}$ / W_5 / a_9	$L_{5\vee}$ / W_6 / b_1	b_2
					Original Design						
	896	696	1022	822	1042	842	1022	822	896	696	
	1461	1361	1461	1361	932	750	707	707	750	932	
	1395	1395	1395	1395	1395	1395	1395	1395	1395	648	648
				Measured with or without Predistortion							
Without Predistortion	809	646	1020	822	1048	798	1011	818	809	650	
	1444	1344	1455	1375	971	755	709	715	762	966	
	1412	1415	1409	1413	1412	1416	1411	1412	1418	649	655
Iteration Step 1 (final filter)	861	635	1031	766	1046	787	1022	774	853	644	
	1433	1333	1451	1370	963	761	711	726	750	957	
	1415	1411	1422	1416	1409	1416	1405	1403	1409	645	651

TABLE B5. Ideally designed and measured dimensions for the non-pre-distorted chained-function filter (with plating).

Dimensions (μm)	$L_{1\wedge}$ / $L_{1feed\wedge}$ / a_1	$L_{1\vee}$ / $L_{1feed\vee}$ / a_2	$L_{2\wedge}$ / $L_{2feed\wedge}$ / a_3	$L_{2\vee}$ / $L_{2feed\vee}$ / a_4	$L_{3\wedge}$ / W_1 / a_5	$L_{3\vee}$ / W_2 / a_6	$L_{4\wedge}$ / W_3 / a_7	$L_{4\vee}$ / W_4 / a_8	$L_{5\wedge}$ / W_5 / a_9	$L_{5\vee}$ / W_6 / b_1	b_2
					Original Design						
	724	724	877	877	912	912	877	877	724	724	
	1543	1543	1543	1543	928	724	655	655	724	928	
	1295	1295	1295	1295	1295	1295	1295	1295	1295	648	648
					Measured						
	768	696	858	799	788	847	852	812	744	707	
	1559	1581	1556	1582	944	754	664	664	756	926	
	1256	1266	1256	1269	1267	1267	1265	1267	1258	647	639

TABLE B6. Ideally designed and measured dimensions for the pre-distorted Chebyshev filter (with plating).

Dimensions (µm)	$L_{1\wedge}$	$L_{1\vee}$	$L_{2\wedge}$	$L_{2\vee}$	$L_{3\wedge}$	$L_{3\vee}$	$L_{4\wedge}$	$L_{4\vee}$	$L_{5\wedge}$	$L_{5\vee}$	
	$L_{1feed\wedge}$	$L_{1feed\vee}$	$L_{2feed\wedge}$	$L_{2feed\vee}$	W_1	W_2	W_3	W_4	W_5	W_6	
	a_1	a_2	a_3	a_4	a_5	a_6	a_7	a_8	a_9	b_1	b_2
Original Design											
	796	796	922	922	942	942	922	922	796	796	
	1411	1411	1411	1411	832	650	607	607	650	832	
	1295	1295	1295	1295	1295	1295	1295	1295	1295	648	648
Measured											
	768	728	929	831	969	883	909	842	740	745	
	1433	1454	1444	1467	870	644	616	620	657	846	
	1311	1323	1328	1315	1321	1328	1328	1319	1311	659	654

TABLE B7. Ideally designed and measured dimensions for the pre-distorted chained-function filter (with plating).

Dimensions (µm)	$L_{1\wedge}$	$L_{1\vee}$	$L_{2\wedge}$	$L_{2\vee}$	$L_{3\wedge}$	$L_{3\vee}$	$L_{4\wedge}$	$L_{4\vee}$	$L_{5\wedge}$	$L_{5\vee}$	
	$L_{1feed\wedge}$	$L_{1feed\vee}$	$L_{2feed\wedge}$	$L_{2feed\vee}$	W_1	W_2	W_3	W_4	W_5	W_6	
	a_1	a_2	a_3	a_4	a_5	a_6	a_7	a_8	a_9	b_1	b_2
Original Design											
	724	724	877	877	912	912	877	877	724	724	
	1543	1543	1543	1543	928	724	655	655	724	928	
	1295	1295	1295	1295	1295	1295	1295	1295	1295	648	648
Measured											
	700	663	854	810	887	852	850	805	691	658	
	1609	1602	1592	1583	891	699	657	657	706	889	
	1307	1316	1302	1319	1308	1324	1313	1319	1304	661	656

REFERENCES
[1] C. W. Hull, "Apparatus for production of three-dimensional objects by stereolithography," U.S. Patent 4 575 330, Mar. 11, 1986.

[2] P. T. Timbie, J. Grade, D. van der Weide, B. Maffei, and G. Pisano, "Stereolithographed mm-wave corrugated horn antennas," in *Proc. 36th Int. Conf. Infr., Millim., THz Waves (IRMMW-THz)*, Houston, TX, USA, Oct. 2011, pp. 1–3.

[3] A. von Bieren, E. de Rijk, J.-P. Ansermet, and A. Macor, "Monolithic metal-coated plastic components for mm-wave applications," in *Proc. 39th Int. Conf. Infr., Millim., THz Waves (IRMMW-THz)*, Tuscon, AZ, USA, Sep. 2014, pp. 1–2.

[4] M. D'Auria, W. J. Otter, J. Hazell, B. T. W. Gillatt, C. Long-Collins, N. M. Ridler, and S. Lucyszyn, "3-D printed metal-pipe rectangular waveguides," *IEEE Trans. Compon., Packag., Manuf. Technol.*, vol. 5, no. 9, pp. 1339–1349, Sep. 2015.

[5] S.-H. Shin, X. Shang, N. M. Ridler, and S. Lucyszyn, "Polymer-based 3-D printed 140–220 GHz low-cost quasi-optical components and integrated subsystem assembly," *IEEE Access*, vol. 9, pp. 28020–28038, 2021.

[6] W. J. Otter and S. Lucyszyn, "Hybrid 3-D-printing technology for tunable THz applications," *Proc. IEEE*, vol. 105, no. 4, pp. 756–767, Apr. 2017.

[7] W. J. Otter, N. M. Ridler, H. Yasukochi, K. Soeda, K. Konishi, J. Yumoto, M. Kuwata-Gonokami, and S. Lucyszyn, "3D printed 1.1 THz waveguides," *IET Electron. Lett.*, vol. 53, no. 7, pp. 471–473, Mar. 2017.

[8] *Eravant*. (2021). Accessed: Mar. 23, 2022. [Online]. Available: https://sftp.eravant.com/content/datasheets/SWF-12401340-08-B1.pdf

[9] *Smith Interconnect*. (2021). Accessed: Mar. 23, 2022. [Online]. Available: https://www.smithsinterconnect.com/getmedia/ec90a824-3499-416b-938d-9f482837c7cf/Iris_Bandpass_Filter-FIB

[10] *Eravant*. (2021). Accessed: Mar. 23, 2022. [Online]. Available: https://sftp.eravant.com/content/datasheets/SWF-14428340-06-B1.pdf

[11] *Elmika*. (2021). Accessed: Mar. 23, 2022. [Online]. Available: http://elmika.com/datasheets/filter/Elmika%20DataSheet%20BPF-015E180+-20%202016%2012%2024.pdf

[12] H. Yang, Y. Dhayalan, X. Shang, M. J. Lancaster, B. Liu, H. Wang, M. Henry, and P. G. Huggard, "WR-3 waveguide bandpass filters fabricated using high precision CNC machining and SU-8 photoresist technology," *IEEE Trans. THz Sci. Technol.*, vol. 8, no. 1, pp. 100–107, Jan. 2018.

[13] Y. P. Lim, S. Cheab, S. Soeung, and P. W. Wong, "On the design and fabrication of chained-function waveguide filters with reduced fabrication sensitivity using CNC and DMLS," *Prog. Electromagn. Res. B*, vol. 87, pp. 39–60, 2020.

[14] F. Zhang, C. Guo, Y. Zhang, Y. Gao, B. Liu, M. Shu, Y. Wang, Y. Dong, M. J. Lancaster, and J. Xu, "A 3-D printed bandpass filter using TM$_{211}$-mode slotted spherical resonators with enhanced spurious suppression," *IEEE Access*, vol. 8, pp. 213215–213223, 2020.

[15] J. Li, C. Guo, L. Mao, and J. Xu, "Compact high-Q hemispherical resonators for 3-D printed bandpass filter applications," in *IEEE MTT-S Int. Microw. Symp. Dig.*, Jun. 2017, pp. 1591–1594.

[16] Y. Zhang, F. Zhang, Y. Gao, J. Xu, C. Guo, and X. Shang, "3D printed waveguide step-twist with bandpass filtering functionality," *Electron. Lett.*, vol. 56, no. 11, pp. 527–528, May 2020.

[17] J. Li, C. Guo, J. Xu, and L. Mao, "Lightweight low-cost Ka-band 3-D printed slotted rectangular waveguide bandpass filters," in *Proc. IEEE Int. Symp. Antennas Propag. USNC/URSI Nat. Radio Sci. Meeting*, Jul. 2017, pp. 2647–2648.

[18] Y. Li, J. Li, M. Zhang, H. Wang, J. Xu, and S. Xiao, "A monolithic stereolithography 3-D printed Ka-band spherical resonator bandpass filter," *2018 IEEE Radio Wireless Symp. (RWS)*, Jan. 2018, pp. 56–59.

[19] B. Al-Juboori, J. Zhou, Y. Huang, M. Hussein, A. Alieldin, W. J. Otter, D. Klugmann, and S. Lucyszyn, "Lightweight and low-loss 3-D printed millimeter-wave bandpass filter based on gap-waveguide," *IEEE Access*, vol. 7, pp. 2624–2632, 2019.

[20] X. Shang, P. Penchev, C. Guo, M. J. Lancaster, S. Dimov, Y. Dong, M. Favre, M. Billod, and E. De Rijk, "W-band waveguide filters fabricated by laser micromachining and 3-D printing," *IEEE Trans. Microw. Theory Techn.*, vol. 64, no. 8, pp. 2572–2580, Aug. 2016.

[21] M. Salek, X. Shang, R. C. Roberts, M. J. Lancaster, F. Boettcher, D. Weber, and T. Starke, "W-band waveguide bandpass filters fabricated by micro laser sintering," *IEEE Trans. Circuits Syst. II, Exp. Briefs*, vol. 66, no. 1, pp. 61–65, Jan. 2019.

[22] T. Skaik, M. Salek, Y. Wang, M. J. Lancaster, T. Starke, and F. Boettcher, "180 GHz waveguide bandpass filter fabricated by 3D printing technology," in *Proc. 13th U.K.-Eur.-China Workshop Millimetre-Waves THz Technol. (UCMMT)*, Aug. 2020, pp. 1–3.

[23] T. Skaik, Y. Yu, Y. Wang, P. G. Huggard, P. Hunyor, and H. Wang, "3D printed microwave components for frequencies above 100 GHz," in *IEEE MTT-S Int. Microw. Symp. Dig.*, Nov. 2021, pp. 246–248.

[24] G. Matthaei, L. Young, and E. M. T. Jones, *Microwave Filters, Impedance-Matching Networks and Coupling Structures*, Norwood, MA, USA: Artech House, 1980.

[25] M. Guglielmi and G. Connor, "Chained function filters," *IEEE Microw. Guided Wave Lett.*, vol. 7, no. 12, pp. 390–392, Dec. 1997.

[26] C. E. Chrisostomidis and S. Lucyszyn, "On the theory of chained-function filters," *IEEE Trans. Microw. Theory Techn.*, vol. 53, no. 10, pp. 3142–3151, Oct. 2005.

[27] C. E. Chrisostomidis and S. Lucyszyn, "Seed function combination selection for chained function filters," *IET Microw., Antennas Propag.*, vol. 4, no. 6, pp. 799–807, Jun. 2010.

[28] C. E. Chrisostomidis, M. Guglielmi, P. Young, and S. Lucyszyn, "Application of chained functions to low-cost microwave band-pass filters using standard PCB etching techniques," in *Proc. 30th Eur. Microw. Conf.*, Oct. 2000, pp. 1–4.

[29] Y. P. Lim, Y. L. Toh, S. Cheab, S. Lucyszyn, and P. W. Wong, "Coupling matrix synthesis and design of a chained-function waveguide filter," in *Proc. Asia–Pacific Microw. Conf. (APMC)*, Nov. 2018, pp. 103–105.

[30] Y. P. Lim, Y. L. Toh, S. Cheab, G. S. Ng, and P. W. Wong, "Chained-function waveguide filter for 5G and beyond," in *Proc. IEEE Region 10th Conf. (TENCON)*, Oct. 2018, pp. 0107–0110.

[31] Y. Leong, S. Cheab, S. Soeung, and P. W. Wong, "A new class of dual-band waveguide filters based on Chebyshev polynomials of the second kind," *IEEE Access*, vol. 8, pp. 28571–28583, 2020.

[32] G. S. Ng, S. Cheab, P. W. Wong, and S. Soeung, "Synthesis of chained-elliptic function waveguide bandpass filter with high rejection," *Prog. Electromagn. Res. C*, vol. 99, pp. 61–75, 2020.

[33] N. Stojanović, N. Stamenković, and I. Krstić, "Chained-function filter synthesis based on the legendre polynomials," *Circuits, Syst., Signal Process.*, vol. 37, no. 5, pp. 2001–2020, May 2018.

[34] G. Perenic, N. Stamenkovic, N. Stojanovic, and N. Denic, "Chained-function filter synthesis based on the modified Jacobi polynomials," *Radioengineering*, vol. 27, no. 4, pp. 1112–1118, Sep. 2018.

[35] D. Stephens, P. R. Young, and I. D. Robertson, "Millimeter-wave substrate integrated waveguides and filters in photoimageable thick-film technology," *IEEE Trans. Microw. Theory Techn.*, vol. 53, no. 12, pp. 3832–3838, Dec. 2005.

[36] R. J. Cameron, C. M. Kudsia, and R. R. Mansour, *Microwave Filters for Communication Systems: Fundamentals Design and Applications*. New York, NY, USA: Wiley, 2018.

[37] X. Shang, W. Xia, and M. J. Lancaster, "The design of waveguide filters based on cross-coupled resonators," *Microw. Opt. Technol. Lett.*, vol. 56, no. 1, pp. 3–8, Jan. 2014.

[38] *Precision Prototyping on Your Desktop*. Stratasys. Accessed: Mar. 23, 2022. [Online]. Available: https://www.stratasys.com/3d-printers/objet30

[39] *Fusion 360*. Autodesk. Accessed: Mar. 23, 2022. [Online]. Available: https://www.autodesk.co.U.K./products/fusion-360/overview

[40] *Chitubox*. Accessed: Mar. 23, 2022. [Online]. Available: https://www.chitubox.com/en

[41] *Elegoo Mars*. Elegoo. Accessed: Mar. 23, 2022. [Online]. Available: https://www.elegoo.com/products/elegoo-mars-2-pro-mono-lcd-3d-printer

[42] *Calibration Targets*. Thorlabs. Accessed: Mar. 23, 2022. [Online]. Available: https://www.thorlabs.com/newgrouppage9.cfm?objectgroup_id=7502

[43] N. Shoaib, N. M. Ridler, and M. J. Salter, "Commissioning of the NPL WR-05 waveguide network analyser system for S-parameter measurements from 140 GHz to 220 GHz," Nat. Phys. Lab., Teddington, U.K., NPL Rep. TQE 12, Mar. 2015.

[44] I. Hunter, *Theory and Design of Microwave Filters*. London, U.K.: Institution of Engineering and Technology, 2001.

LIYAN ZHU received the B.Eng. degree in electronic science and technology from the Huazhong University of Science and Technology (HUST), Wuhan, China, in 2018, and the M.Sc. degree in telecommunications from the University College London (UCL), London, U.K., in 2019. He is currently pursuing the Ph.D. degree with the Department of Electrical and Electronic Engineering, Imperial College London, London. His research interests include the design, fabrication, and sensitivity analysis of microwave components using additive manufacturing techniques.

ROSHAN PAYAPULLI was born in Bengaluru, India, in 1995. He received the M.Eng. degree in electrical and electronic engineering from the Imperial College London, London, U.K., in 2018, where he is currently pursuing the Ph.D. degree with the Department of Electrical and Electronic Engineering.

His research interests include designing and manufacturing lightweight and low-cost waveguide components and systems for microwave and millimeter-wave applications using additive manufacturing techniques.

SANG-HEE SHIN (Member, IEEE) was born in Seoul, South Korea, in 1992. He received the M.Eng. degree in aeronautical engineering and the Ph.D. degree in electrical and electronic engineering from Imperial College London, London, U.K., in 2018 and 2022, respectively.

He joined the Department of Electromagnetic and Electrochemical Technologies, U.K.'s National Physical Laboratory, as a Higher Research Scientist. His research interests include designing and manufacturing RF and quasi-optical devices for microwave and millimeter-wave applications using additive manufacturing techniques.

MANOJ STANLEY (Member, IEEE) received the Ph.D. degree in electrical engineering from the University of Liverpool, in 2019. After the completion of his Ph.D., he joined the Electromagnetic Technologies Group, U.K.'s National Physical Laboratory, as a Higher Research Scientist. He has supported the development of next-generation computing and communications technologies and high-frequency electronics applications. This includes design and characterization of devices at RF and terahertz frequencies, RF metrology for quantum computing applications, material and channel characterization for 5G and beyond communication. He is developing high-frequency metrology capabilities to characterize superconducting quantum integrated circuits at milli-Kelvin temperatures. He is the Operations Officer for European Microwave Week 2021.

NICK M. RIDLER (Fellow, IEEE) received the B.Sc. degree from the King's College London, University of London, London, U.K., in 1981. He is currently the Head of Science with the Electromagnetic and Electrochemical Technologies Department, U.K.'s National Physical Laboratory (NPL). He is an NPL Fellow, an Honorary Professor at the Universities of Glasgow and Liverpool, U.K., and a Visiting Professor at the Universities of Kent, Leeds and Surrey, U.K. He is also a Non-Executive Director of LA Techniques Ltd. He has more than 35 years' experience working in industrial, government and academic research establishments. His research interest includes precision high-frequency electromagnetic measurement (from 1 kHz to 1 THz). He is a fellow of the Institution of Engineering and Technology (IET) and a fellow of the Institute of Physics (IOP). He is the General Chair of the European Microwave Week 2021.

STEPAN LUCYSZYN (Fellow, IEEE) received the Ph.D. degree in electronic engineering from the King's College London, University of London, London, U.K., in 1992, and the D.Sc. degree (higher doctorate) in millimetre-wave and terahertz electronics from the Imperial College London, London, in 2010.

He is currently a Professor of millimetre-wave systems with the Imperial College London. He has coauthored well over 200 articles and 12 book chapters in applied physics and electronic engineering. He was made a fellow of the Institution of Electrical Engineers, U.K., and the Institute of Physics, U.K., in 2005. In 2008, he became a fellow of the Electromagnetics Academy, USA. He was appointed as an IEEE Distinguished Microwave Lecturer, from 2010 to 2013. He co-founded the Imperial College London spin-out company Drayson Wireless Ltd., in 2014. In 2022, for their work on 3D printing, he and his team at Imperial College London won Junkosha's Inaugural Technology Innovator of the Year Award for the Microwave and Millimeter Wave Category.

● ● ●